Supplementary Information for

Rising natural aerosols drive marine radiative forcing as pollution declines

Vaios Moschos[†*], Emmanuel Chevassus[†], Kirsten N. Fossum[†], Lu Lei[†], Jakob B. Pernov[§], Ruhi S. Humphries[⊥], Melita D. Keywood[⊥], Colin O'Dowd[†], Darius Ceburnis[†], and Jurgita Ovadnevaite[†*]

[†] School of Natural Sciences, Ryan Institute's Centre for Climate and Air Pollution Studies, University of Galway, Galway, Ireland

[§] School of Earth and Atmospheric Sciences, Queensland University of Technology, Brisbane, Australia

[⊥] Environment Research Unit, Commonwealth Scientific and Industrial Research Organisation (CSIRO), Melbourne, Victoria, Australia

The SI includes:

Figures S1 to S7

Tables S1 to S2

Supplementary Text

SI References

Number of pages: 24

SI Figures

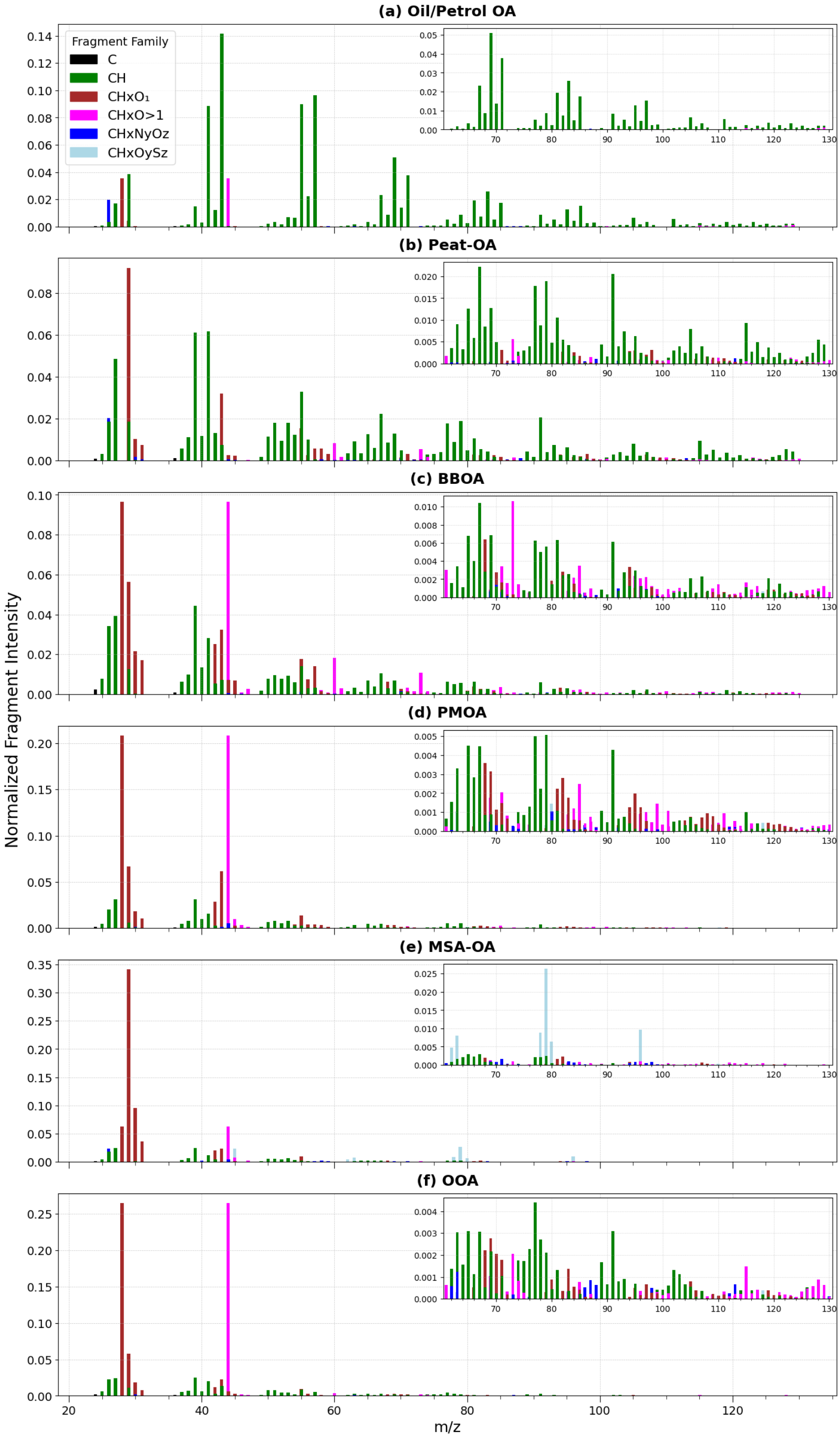

Figure S1. Mass spectral profiles of OA factors identified via AMS-PMF analysis at MHD. The inset for each panel zooms in to the low-intensity fragments at *m/z* > 60.

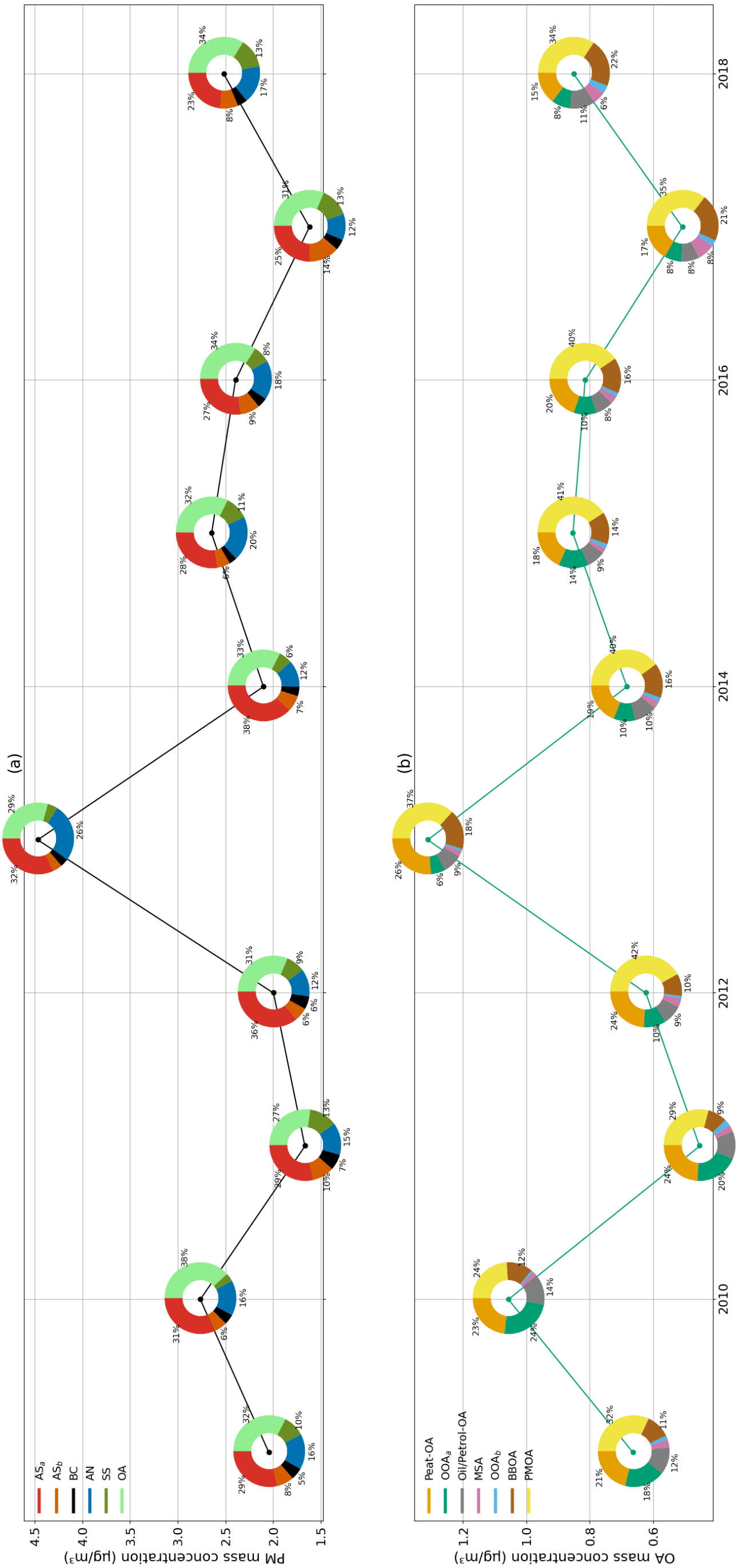

Figure S2. Decadal-scale evolution of yearly averaged speciated PM & OA at MHD from monthly values (years 2008 and 2019 are not shown here due to incomplete annual coverage). The pie charts represent the contribution of each species and PMF factor to the yearly average.

Figure S3. STL decomposition results for all aerosol components at MHD. The STL inputs (imputed, continuous time series) are shown as dashed lines in panels (a). In panels (d), some aerosol components exhibited no residual autocorrelation after STL; for these components, no autocorrelation correction (Text S3) was applied to the STL Residuals (panels d), and the dashed and solid lines overlap.

AS_a

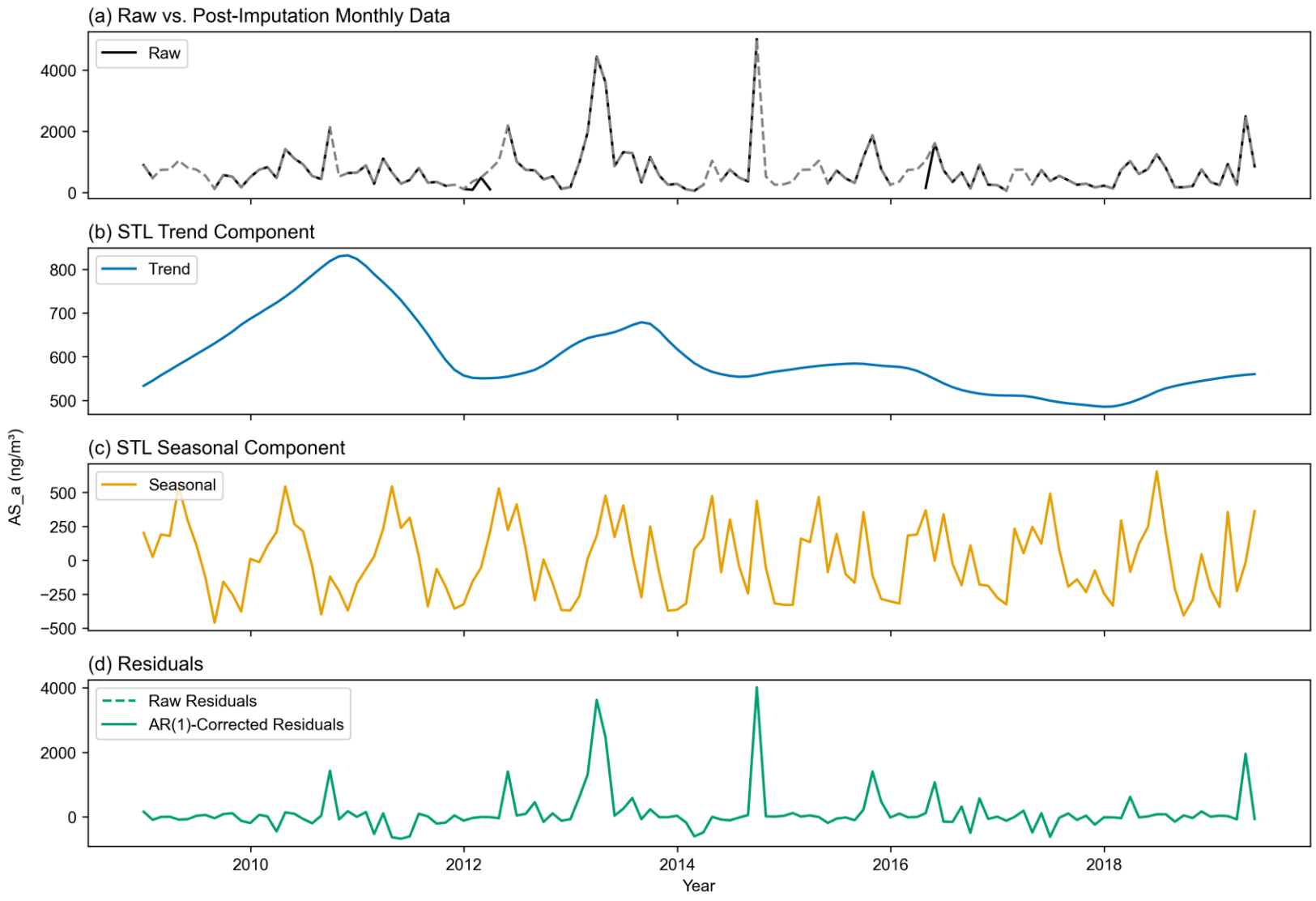

Peat-OA

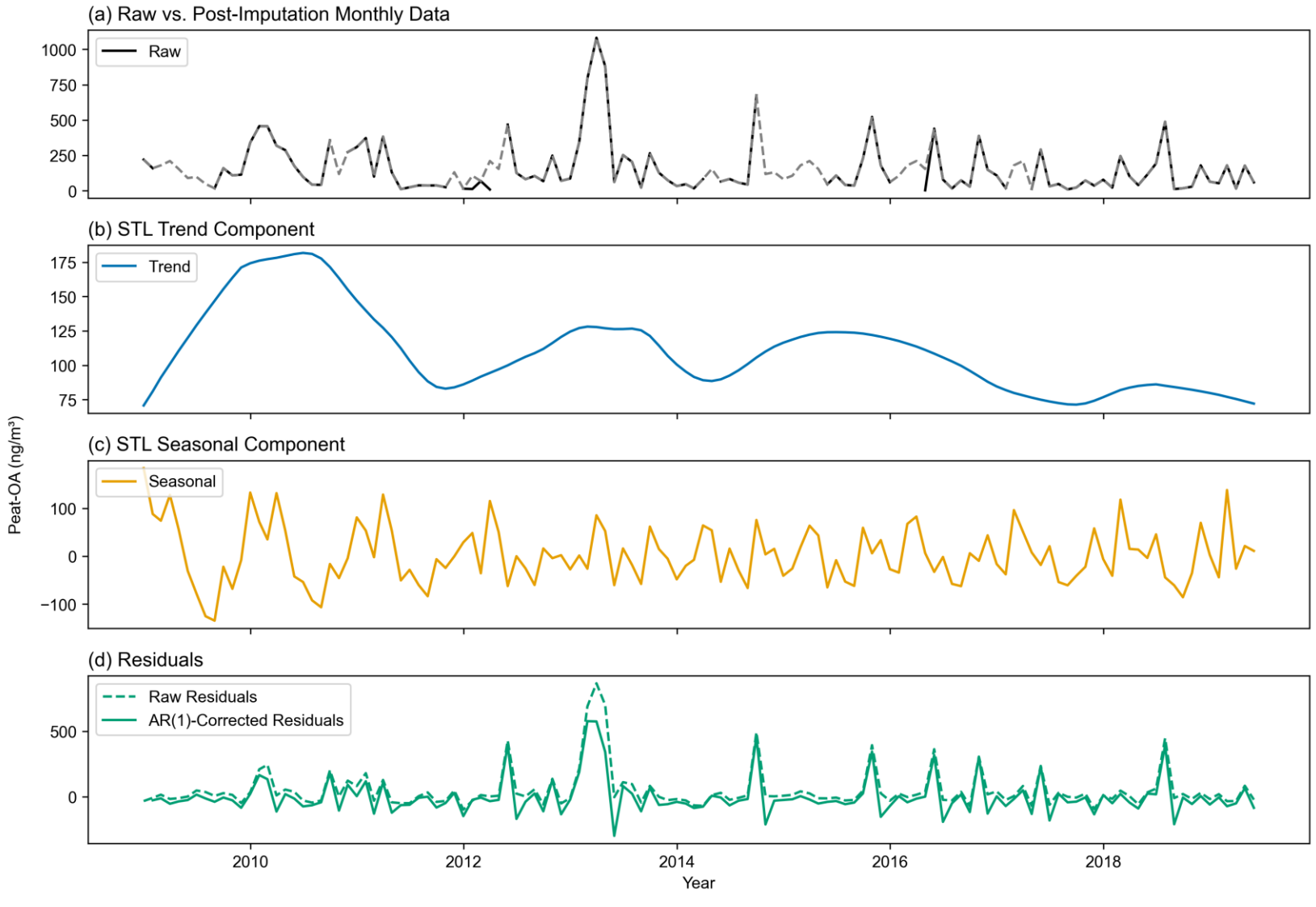

Oil_Petrol-OA

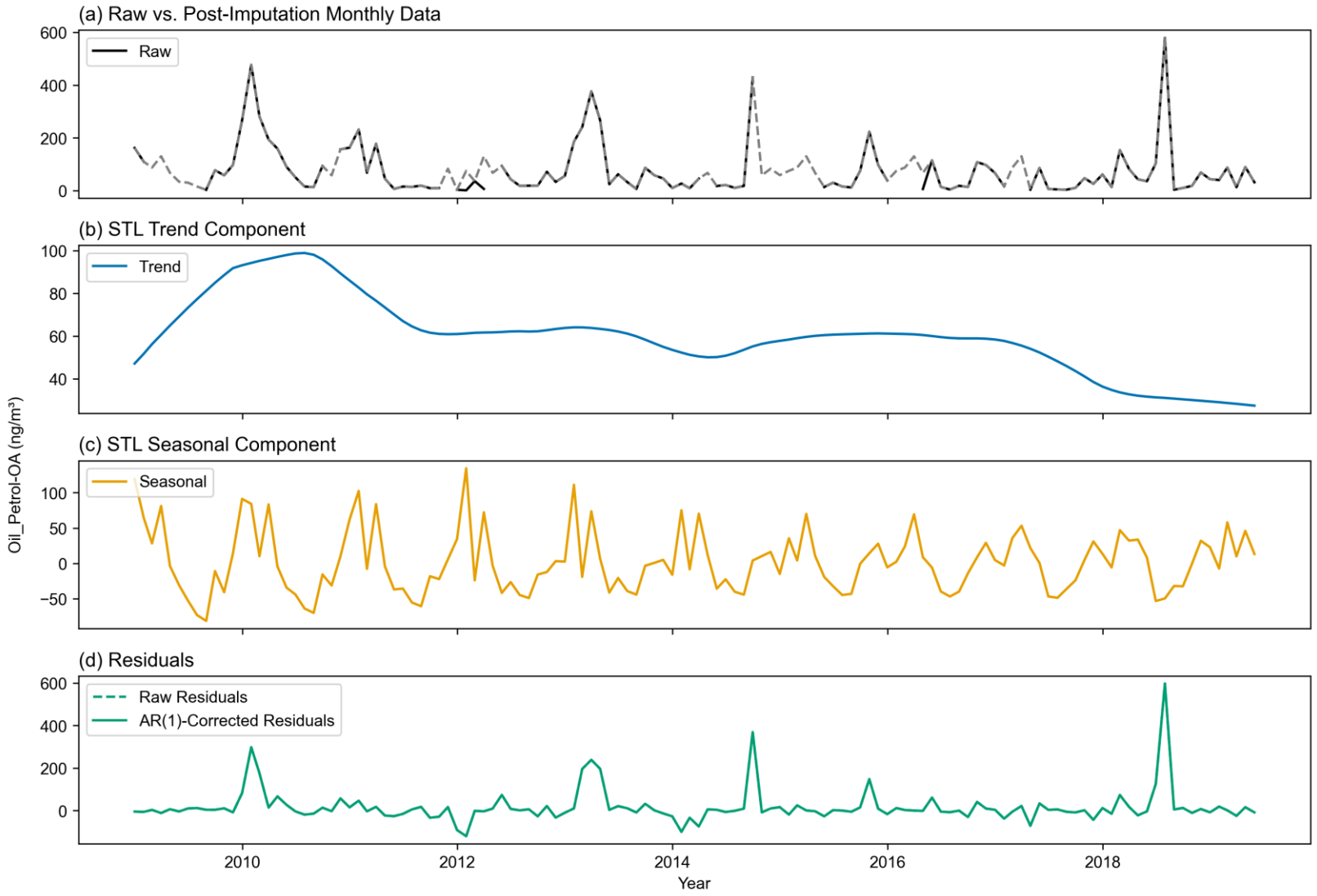

OOA_a

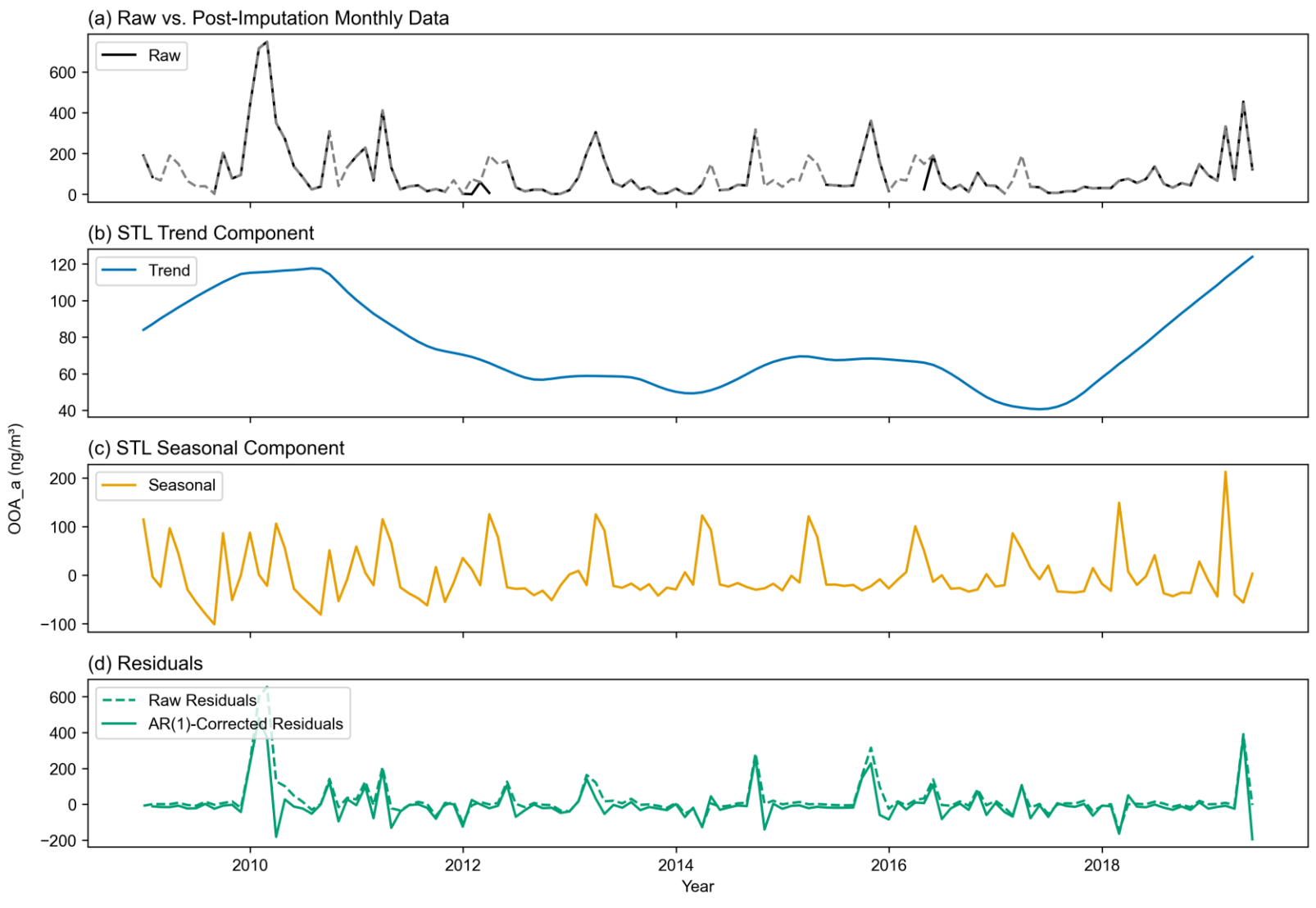

BC

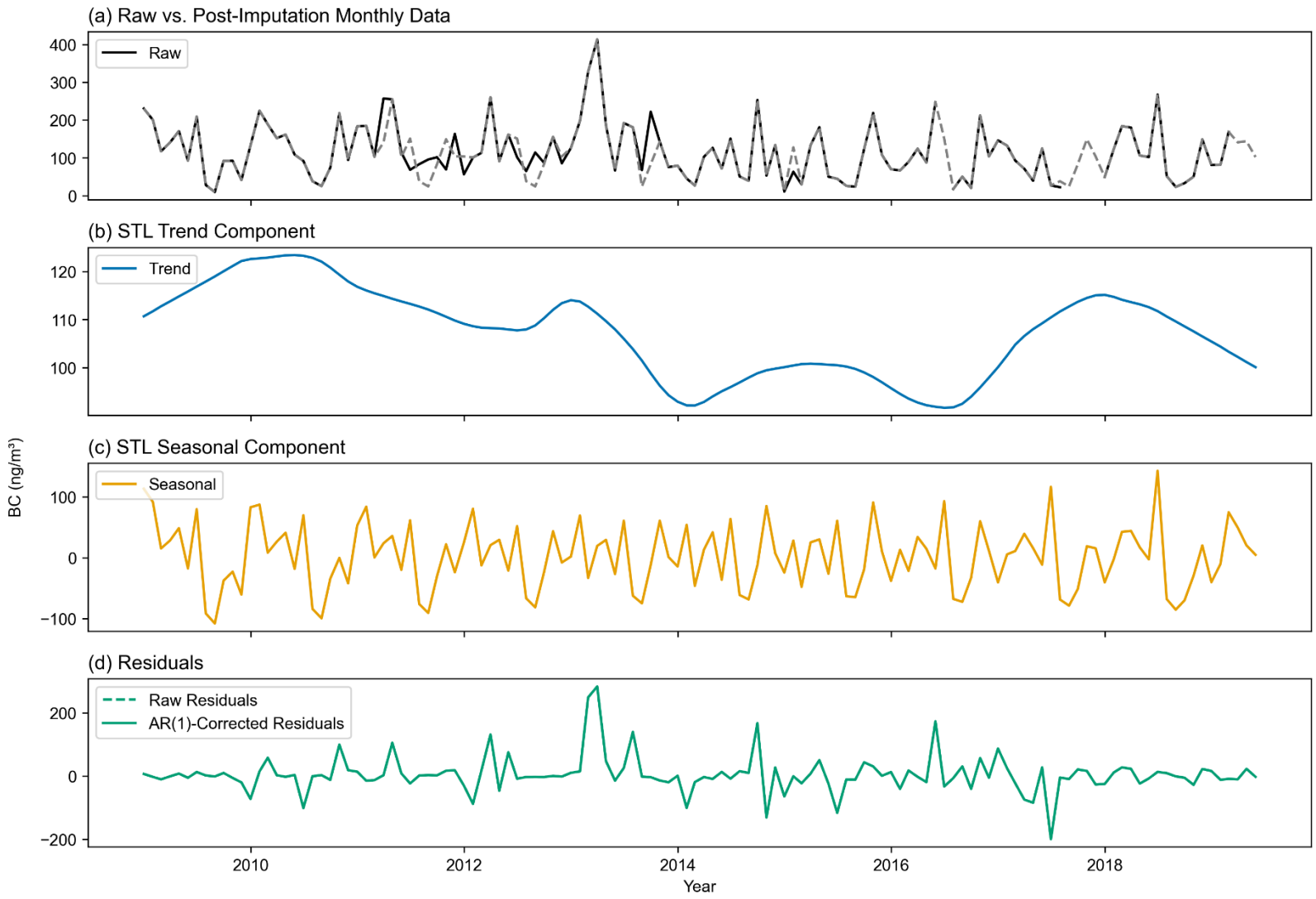
(a) Raw vs. Post-Imputation Monthly Data
Raw
400
300
200
100
0
(b) STL Trend Component
Trend
120
110
100
(c) STL Seasonal Component
Seasonal
100
0
−100
BC (ng/m³)
(d) Residuals
Raw Residuals
AR(1)-Corrected Residuals
200
0
−200
2010
2012
2014
2016
2018
Year

AN

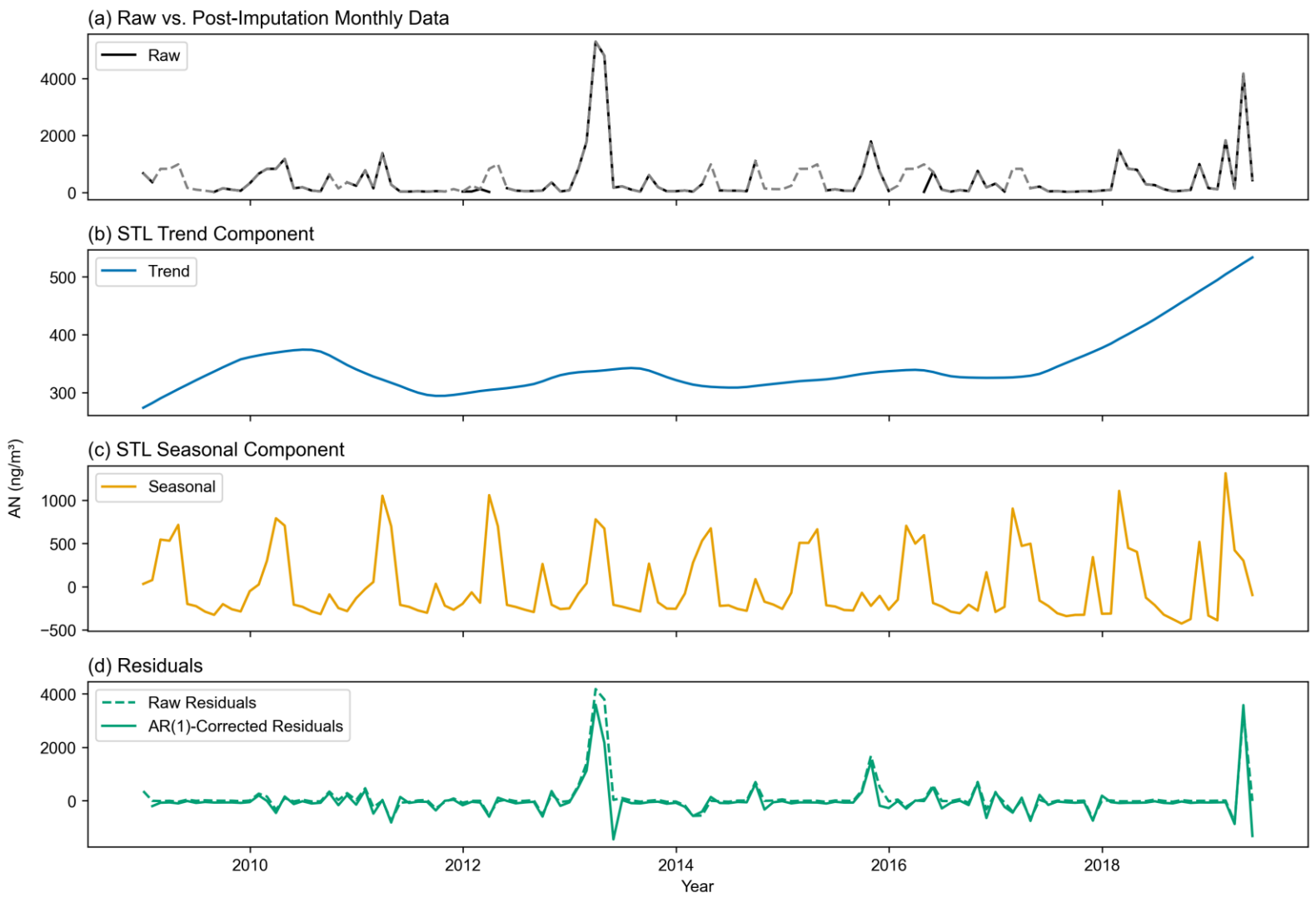
(a) Raw vs. Post-Imputation Monthly Data
Raw
4000
2000
0
(b) STL Trend Component
Trend
500
400
300
(c) STL Seasonal Component
Seasonal
1000
500
0
−500
AN (ng/m³)
(d) Residuals
Raw Residuals
AR(1)-Corrected Residuals
4000
2000
0
2010
2012
2014
2016
2018
Year

BBOA

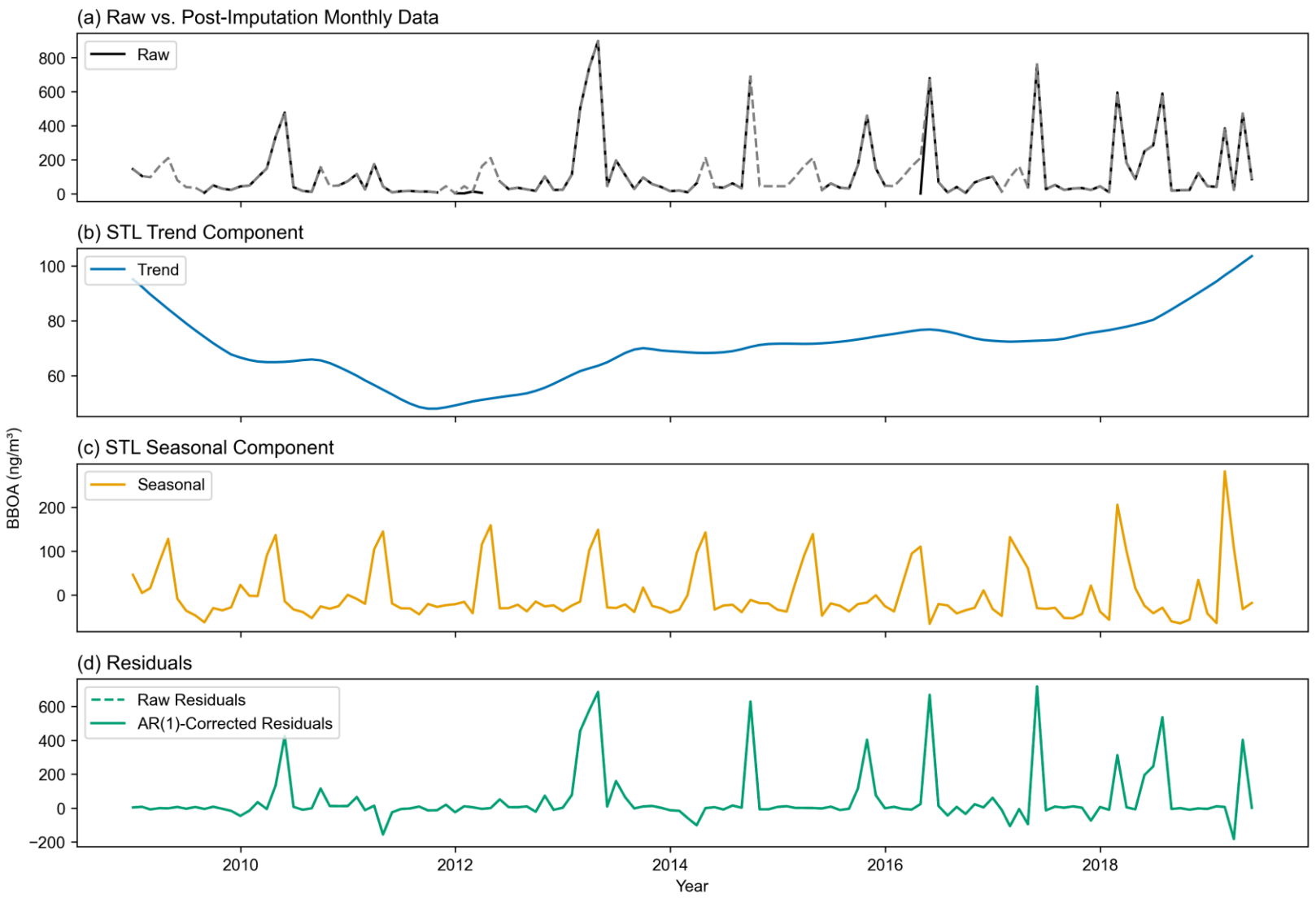
(a) Raw vs. Post-Imputation Monthly Data
Raw
800
600
400
200
0
(b) STL Trend Component
Trend
100
80
60
BBOA (ng/m³)
(c) STL Seasonal Component
Seasonal
200
100
0
(d) Residuals
Raw Residuals
AR(1)-Corrected Residuals
600
400
200
0
−200
2010
2012
2014
2016
2018
Year

MSA

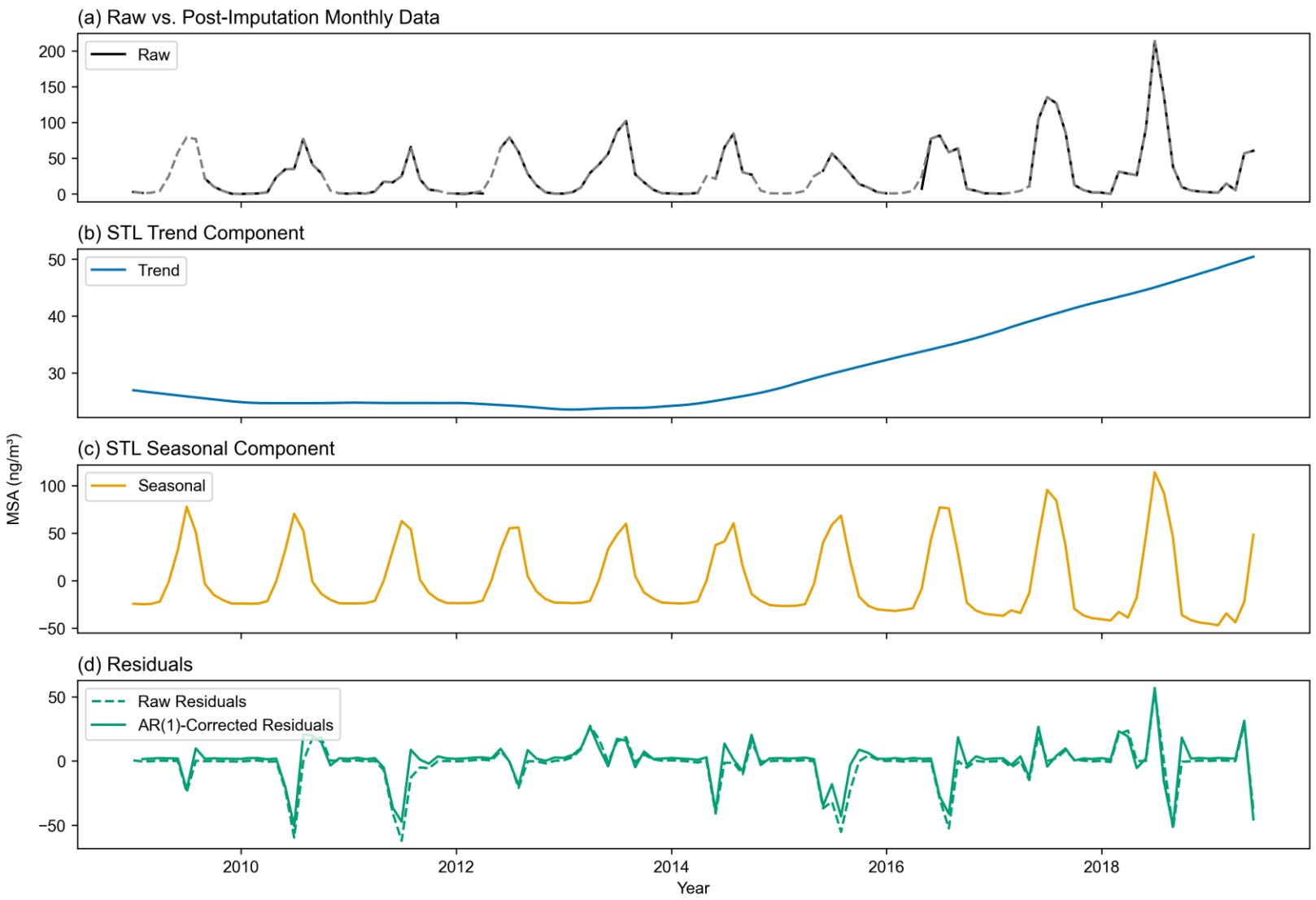
(a) Raw vs. Post-Imputation Monthly Data
Raw
200
150
100
50
0
(b) STL Trend Component
Trend
50
40
30
(c) STL Seasonal Component
Seasonal
MSA (ng/m³)
100
50
0
−50
(d) Residuals
Raw Residuals
AR(1)-Corrected Residuals
50
0
−50
2010
2012
2014
2016
2018
Year

OOA_b

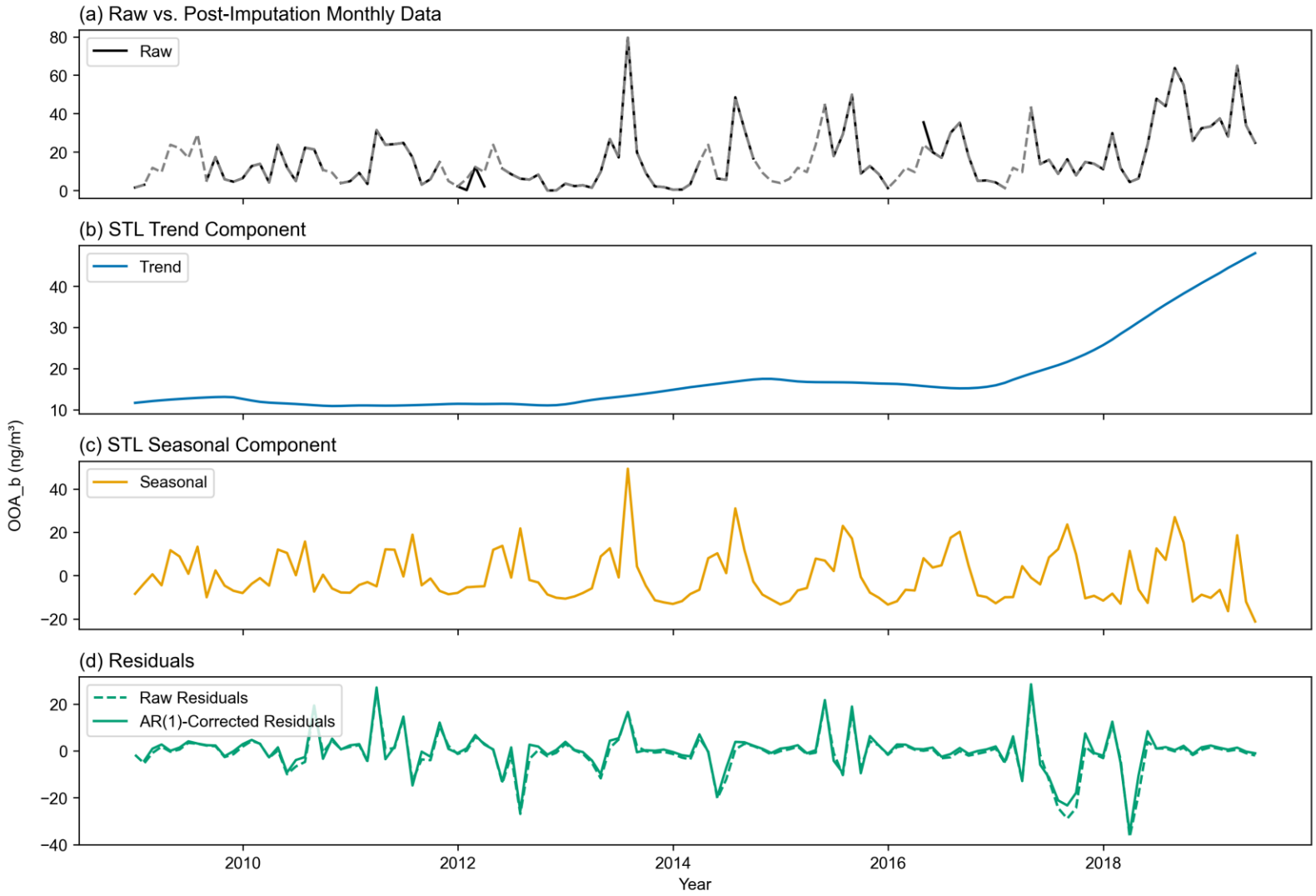
(a) Raw vs. Post-Imputation Monthly Data
Raw
(b) STL Trend Component
Trend
(c) STL Seasonal Component
Seasonal
(d) Residuals
Raw Residuals
AR(1)-Corrected Residuals
OOA_b (ng/m³)
Year

PMOA

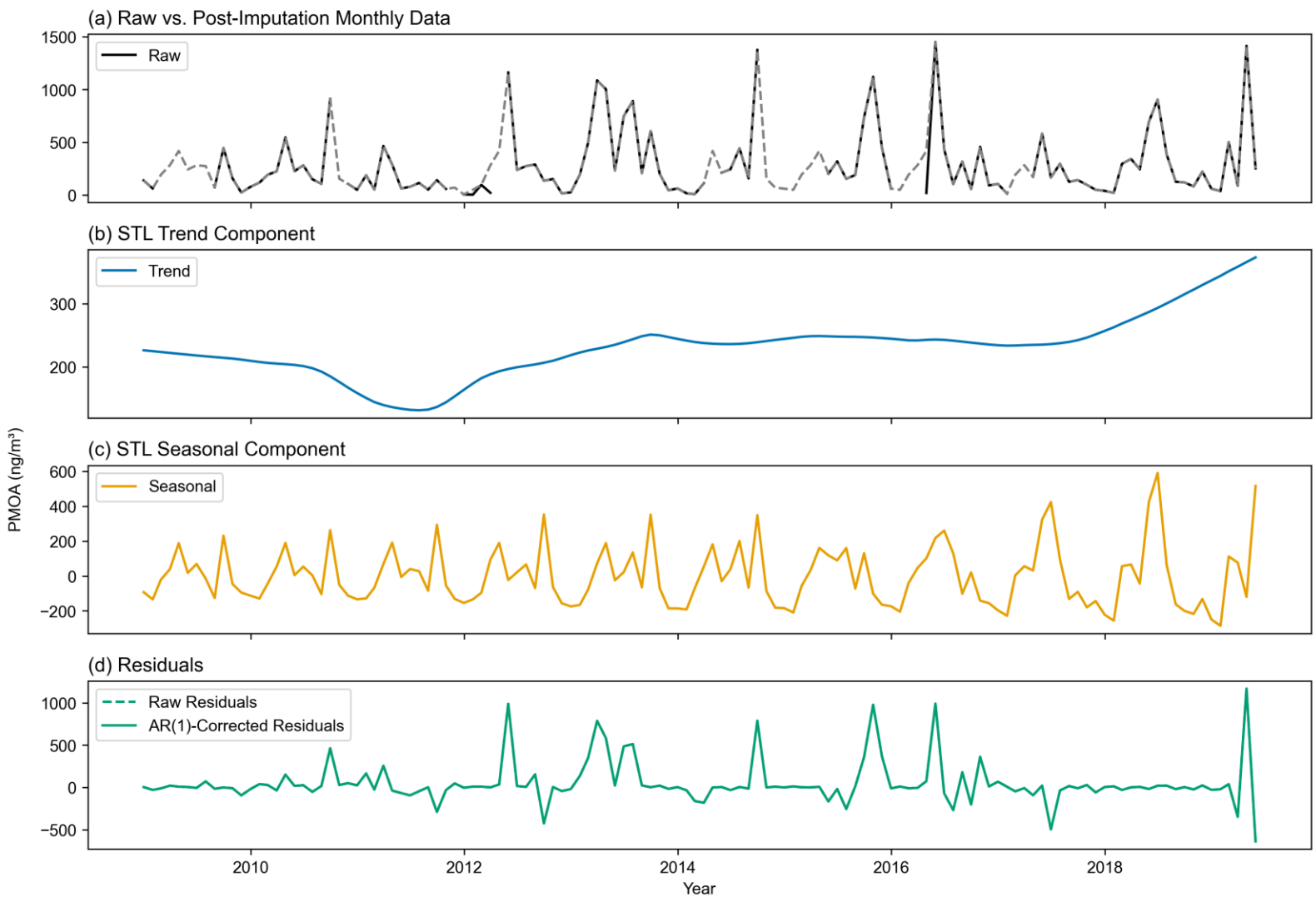
(a) Raw vs. Post-Imputation Monthly Data
Raw
(b) STL Trend Component
Trend
(c) STL Seasonal Component
Seasonal
(d) Residuals
Raw Residuals
AR(1)-Corrected Residuals
PMOA (ng/m³)
Year

AS_b

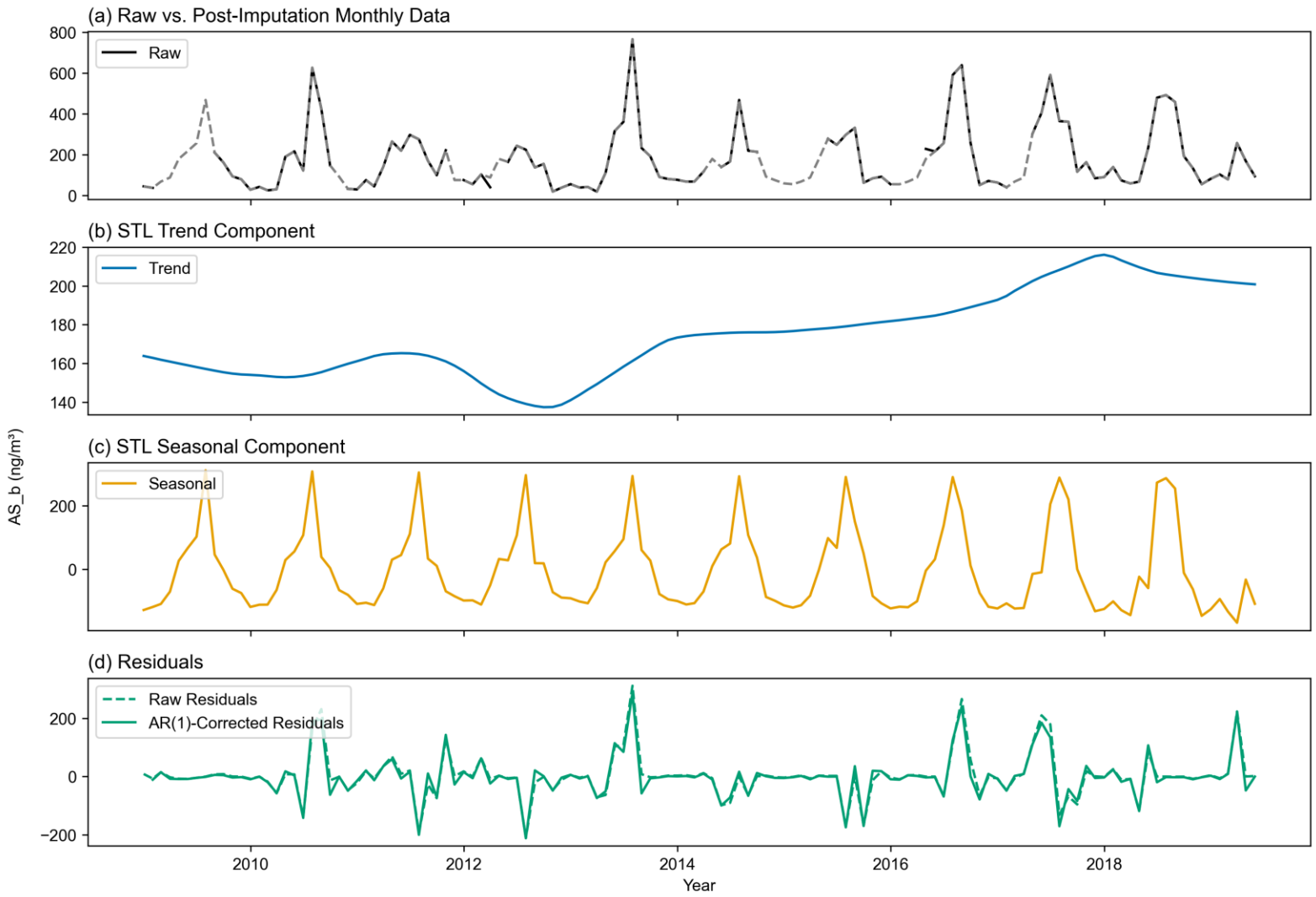
(a) Raw vs. Post-Imputation Monthly Data
Raw
(b) STL Trend Component
Trend
(c) STL Seasonal Component
Seasonal
AS_b (ng/m³)
(d) Residuals
Raw Residuals
AR(1)-Corrected Residuals
Year

SS

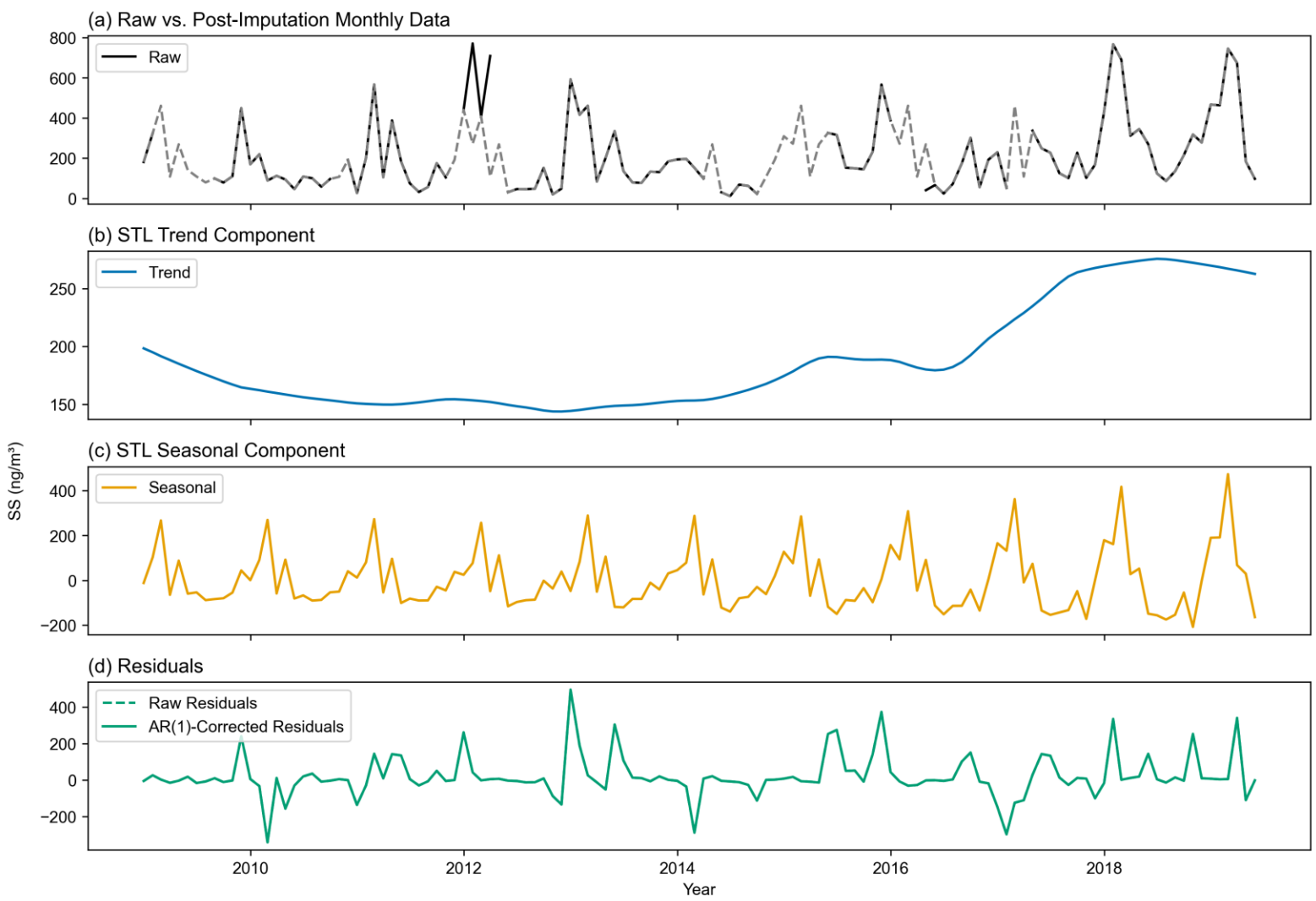
(a) Raw vs. Post-Imputation Monthly Data
Raw
(b) STL Trend Component
Trend
(c) STL Seasonal Component
Seasonal
SS (ng/m³)
(d) Residuals
Raw Residuals
AR(1)-Corrected Residuals
Year

Figure S4. MHD aerosol STL-Trend components' QR τ-grid plots in ng/m^3, or percent change, per year.

AS_a

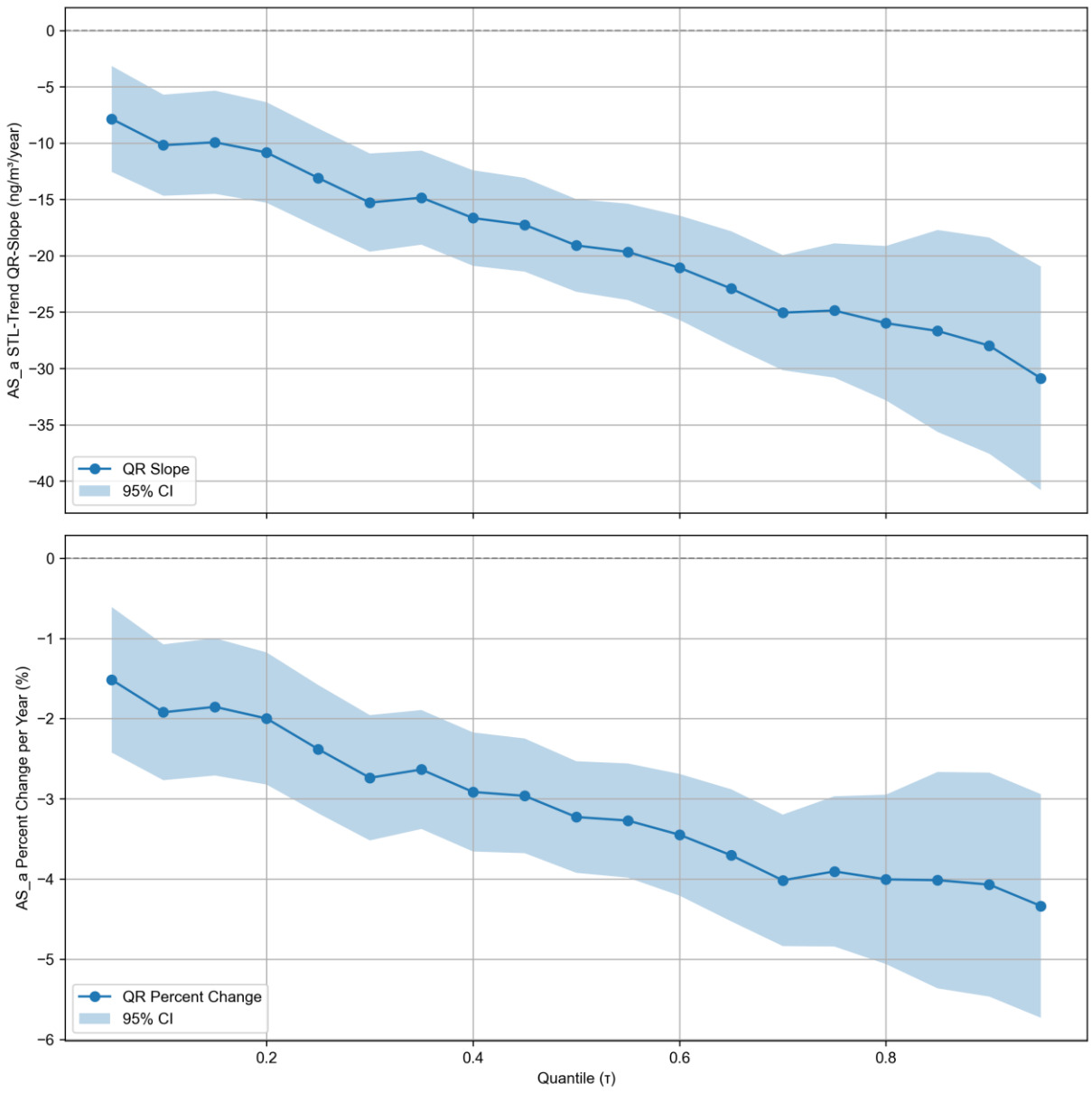

Peat-OA

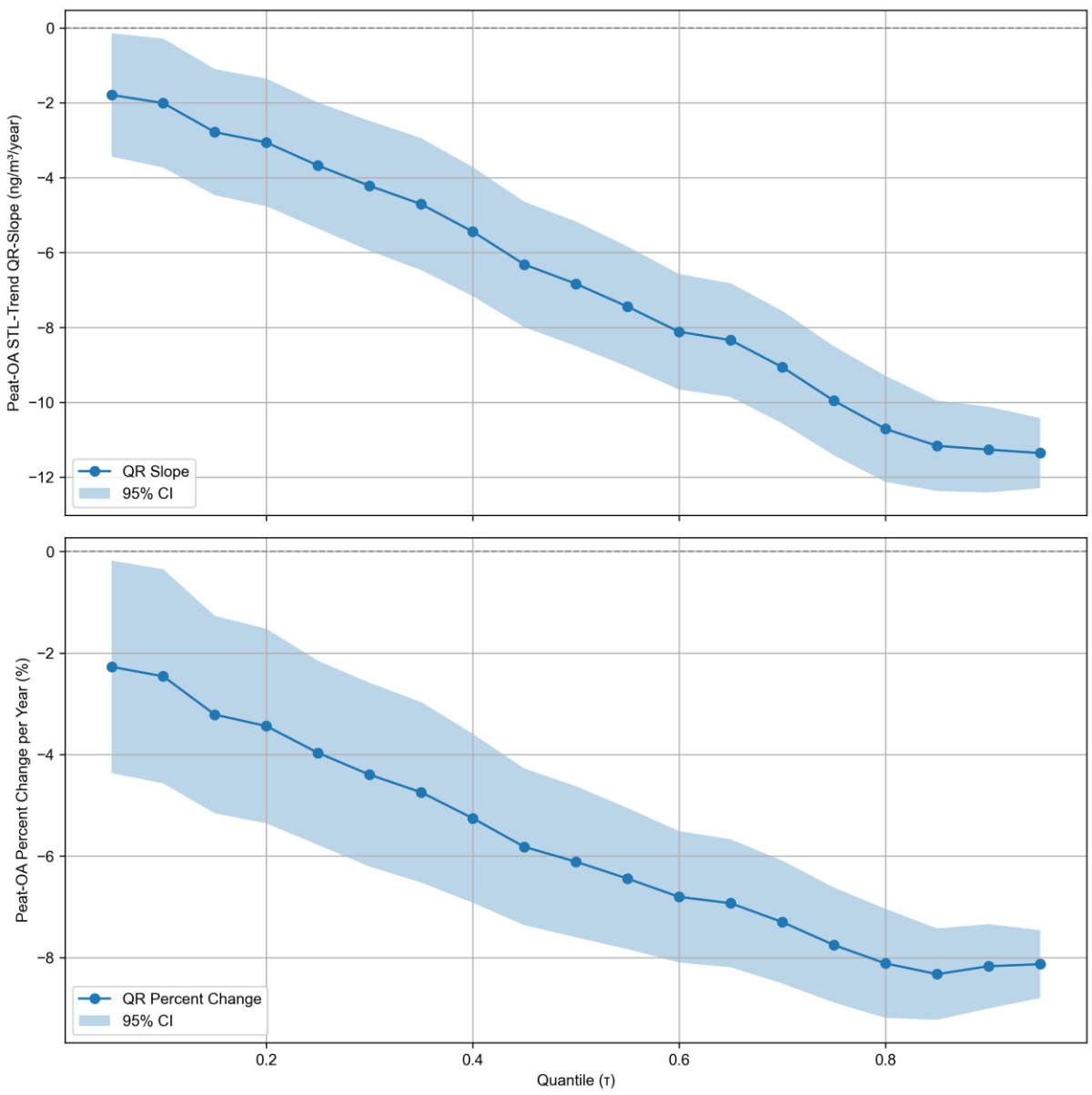

Oil/Petrol-OA

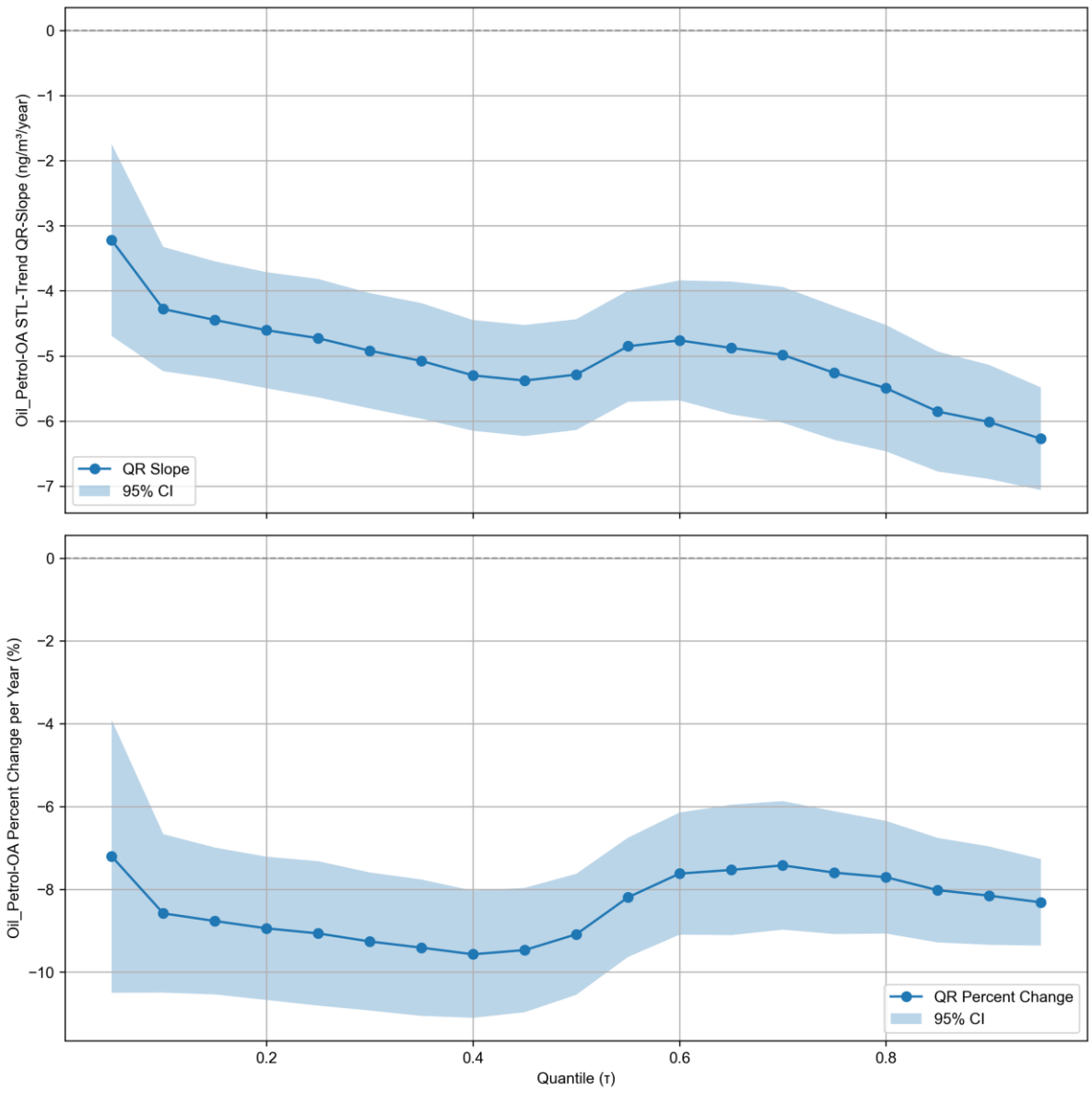

OOA_a

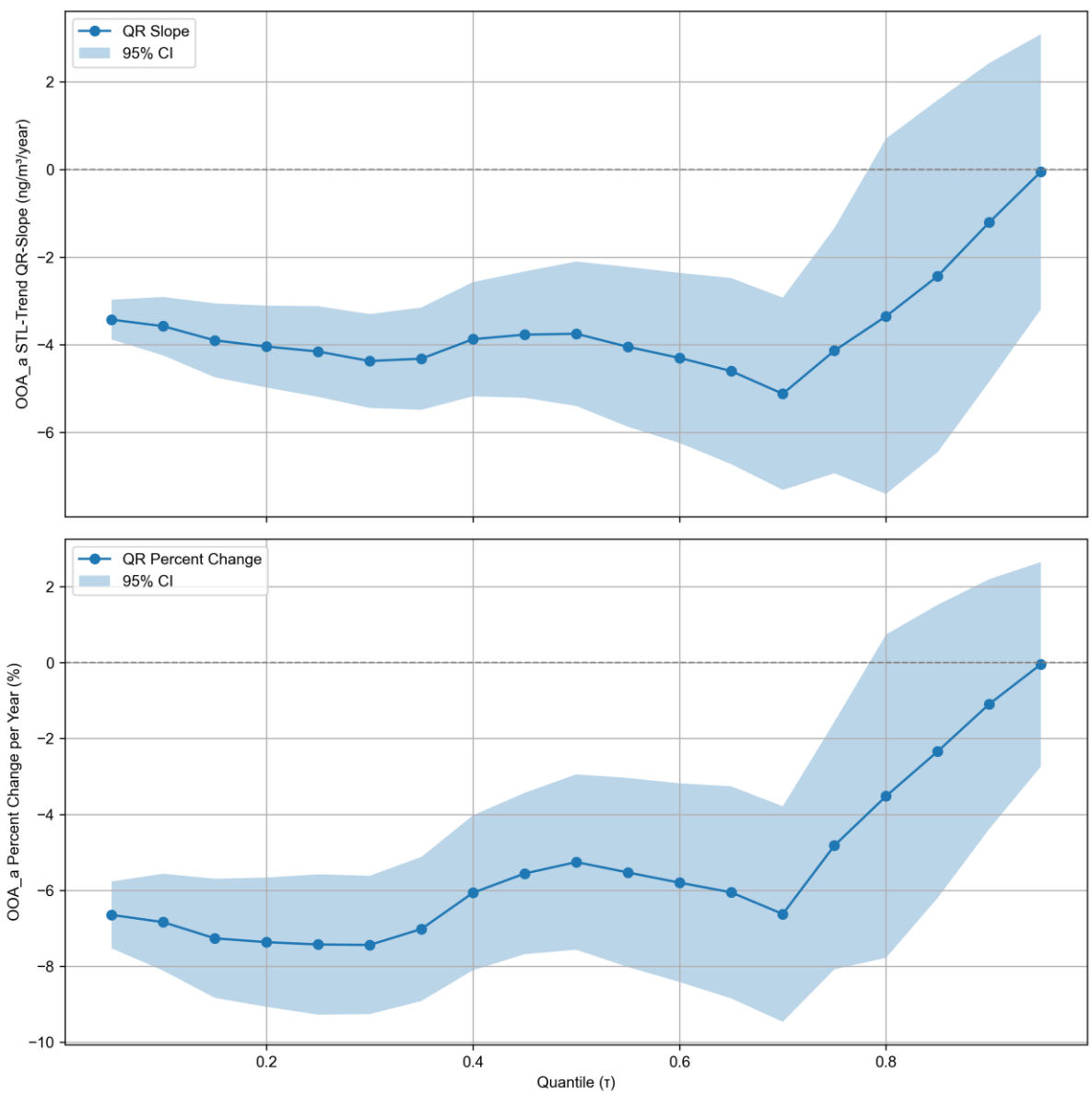

BC

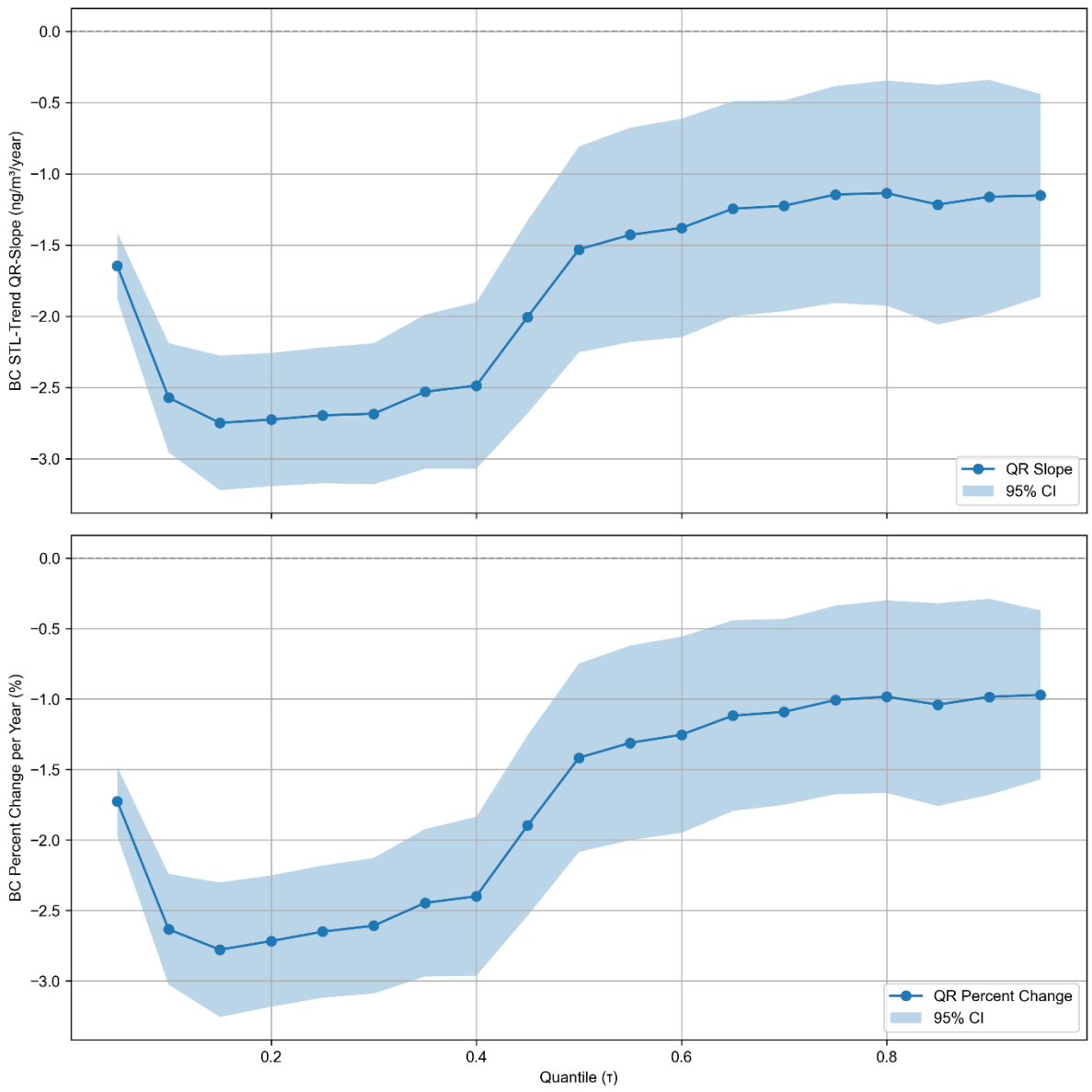
BC STL-Trend QR-Slope (ng/m³/year)
0.0
−0.5
−1.0
−1.5
−2.0
−2.5
−3.0
QR Slope
95% CI
BC Percent Change per Year (%)
0.0
−0.5
−1.0
−1.5
−2.0
−2.5
−3.0
QR Percent Change
95% CI
0.2
0.4
0.6
0.8
Quantile (τ)

AN

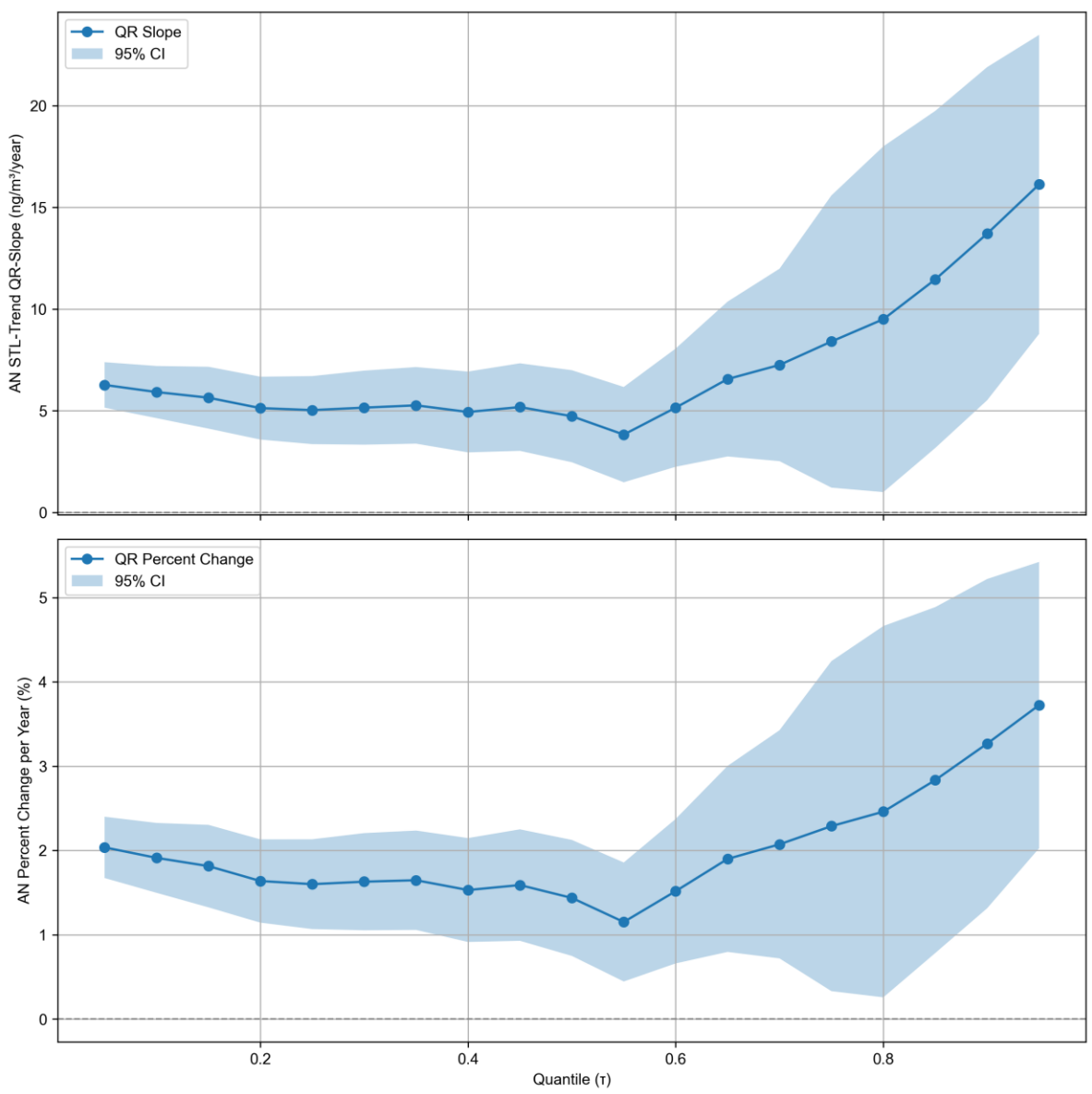
QR Slope
95% CI
AN STL-Trend QR-Slope (ng/m³/year)
20
15
10
5
0
QR Percent Change
95% CI
AN Percent Change per Year (%)
5
4
3
2
1
0
0.2
0.4
0.6
0.8
Quantile (τ)

BBOA

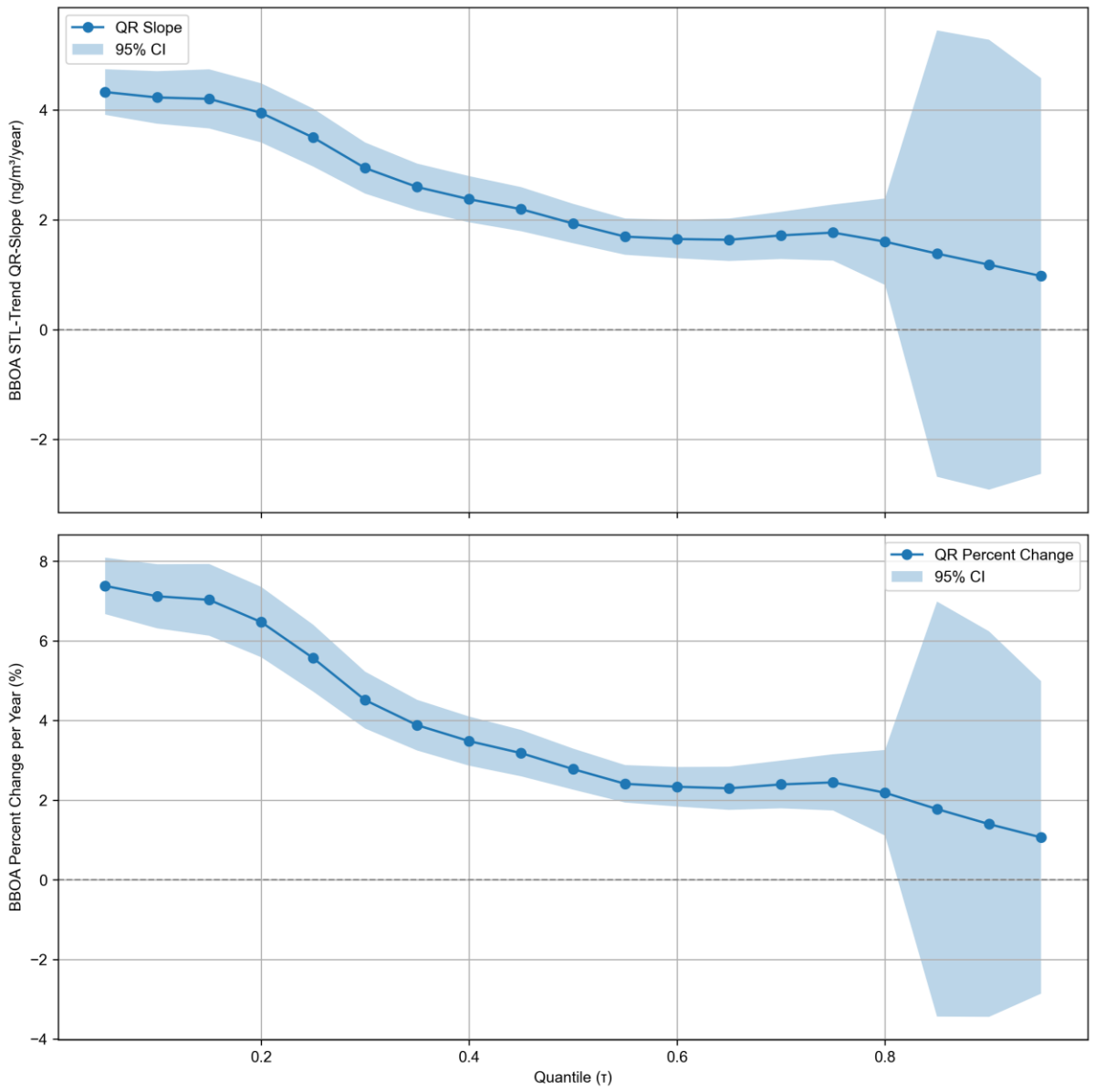
QR Slope
95% CI
BBOA STL-Trend QR-Slope (ng/m³/year)
4
2
0
−2
QR Percent Change
95% CI
BBOA Percent Change per Year (%)
8
6
4
2
0
−2
−4
0.2
0.4
0.6
0.8
Quantile (τ)

MSA

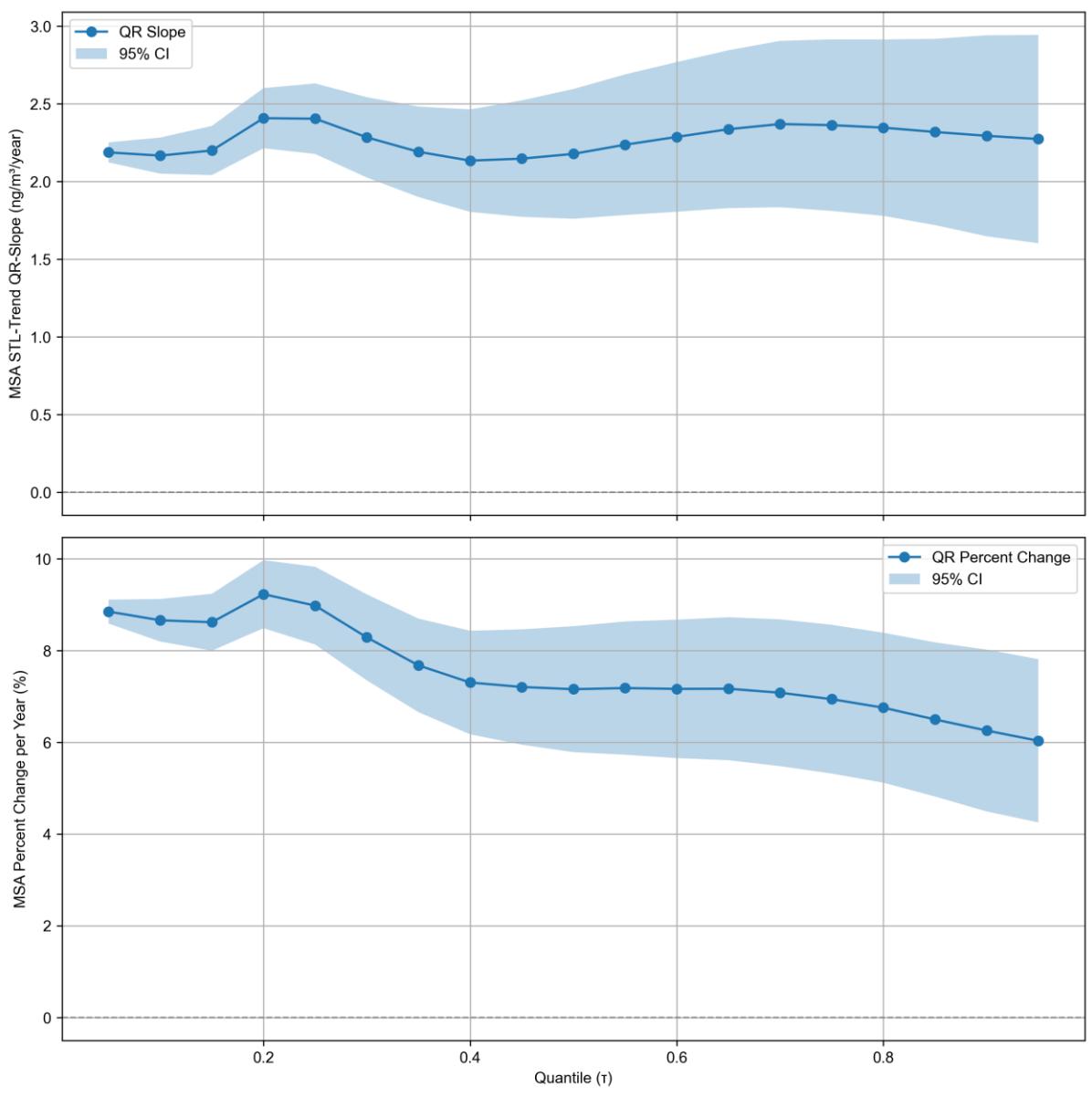
QR Slope
95% CI
MSA STL-Trend QR-Slope (ng/m³/year)
3.0
2.5
2.0
1.5
1.0
0.5
0.0
QR Percent Change
95% CI
MSA Percent Change per Year (%)
10
8
6
4
2
0
0.2
0.4
0.6
0.8
Quantile (τ)

OOA_b

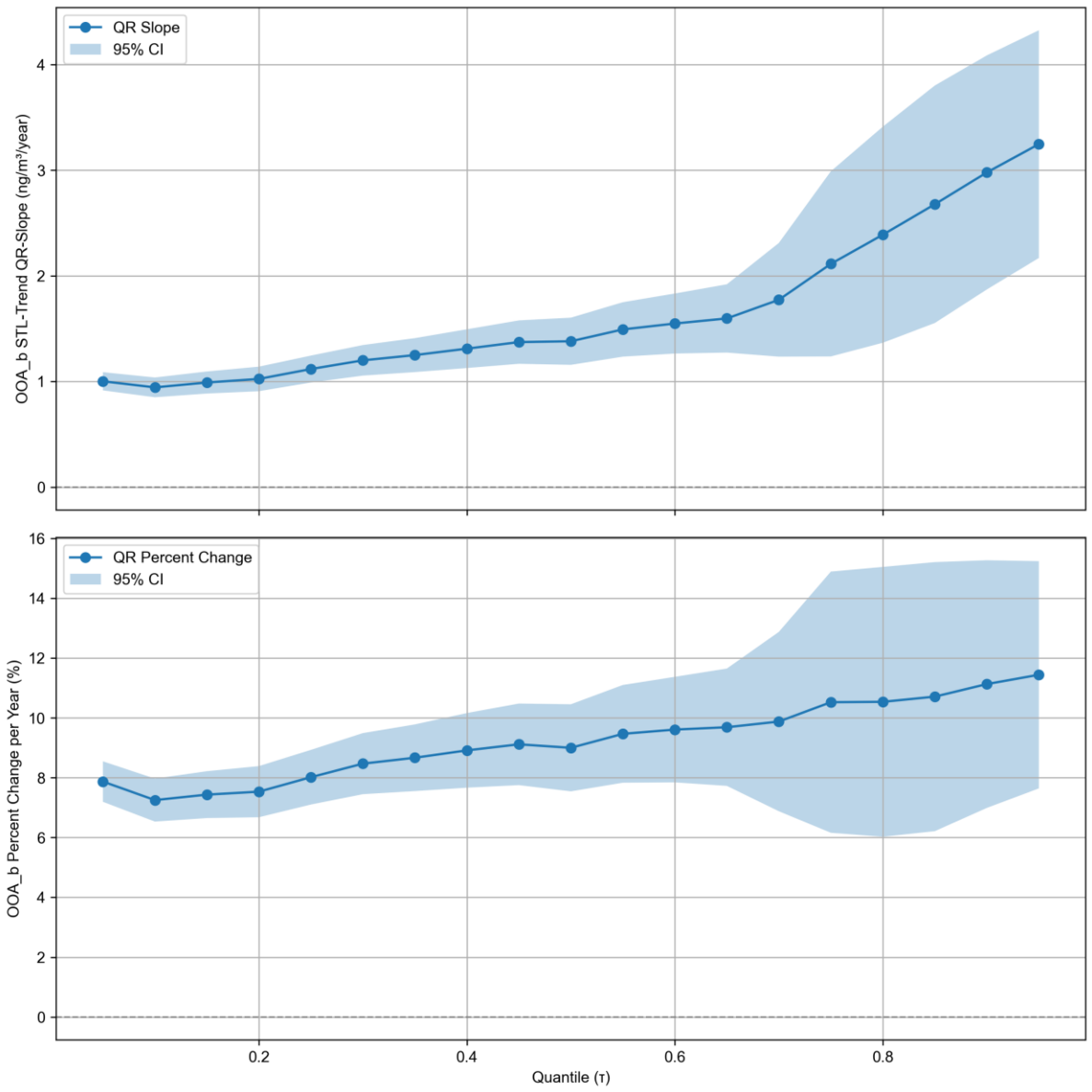
QR Slope
95% CI
OOA_b STL-Trend QR-Slope (ng/m³/year)
0
1
2
3
4
QR Percent Change
95% CI
OOA_b Percent Change per Year (%)
0
2
4
6
8
10
12
14
16
0.2
0.4
0.6
0.8
Quantile (τ)

PMOA

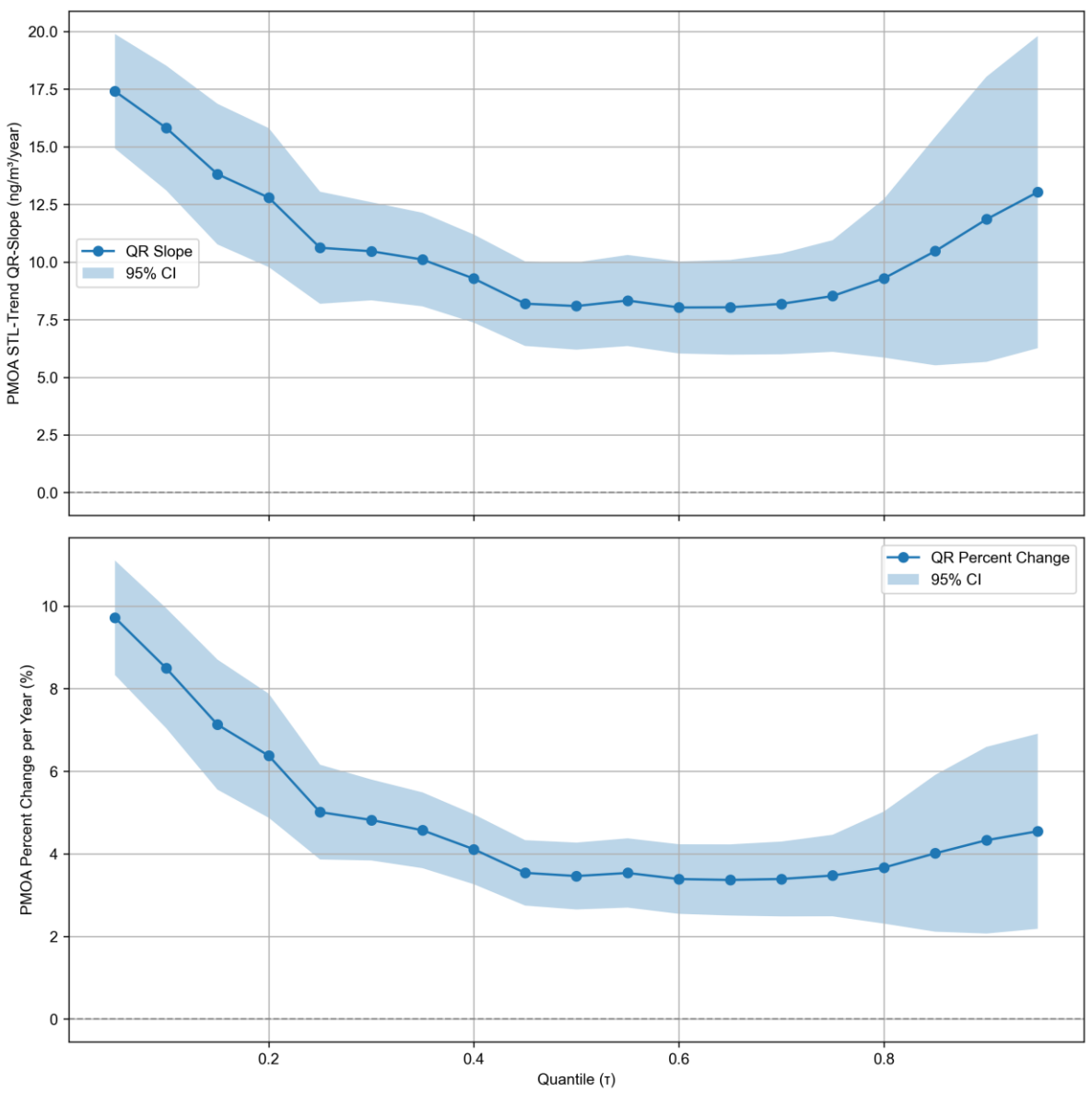
QR Slope
95% CI
PMOA STL-Trend QR-Slope (ng/m³/year)
0.0
2.5
5.0
7.5
10.0
12.5
15.0
17.5
20.0
QR Percent Change
95% CI
PMOA Percent Change per Year (%)
0
2
4
6
8
10
0.2
0.4
0.6
0.8
Quantile (τ)

AS_b

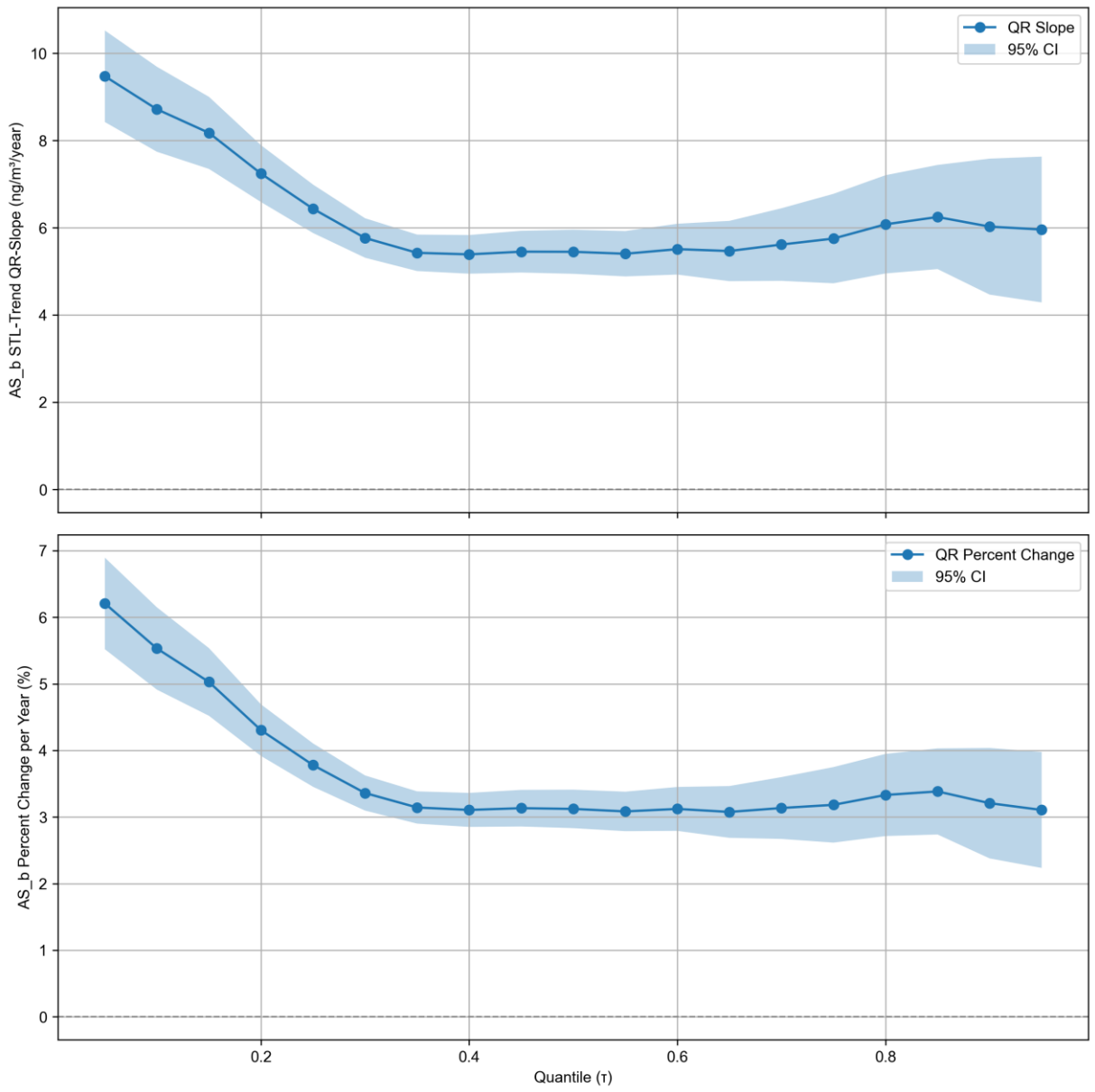
QR Slope
95% CI
AS_b STL-Trend QR-Slope (ng/m³/year)
10
8
6
4
2
0
QR Percent Change
95% CI
AS_b Percent Change per Year (%)
7
6
5
4
3
2
1
0
0.2
0.4
0.6
0.8
Quantile (τ)

SS

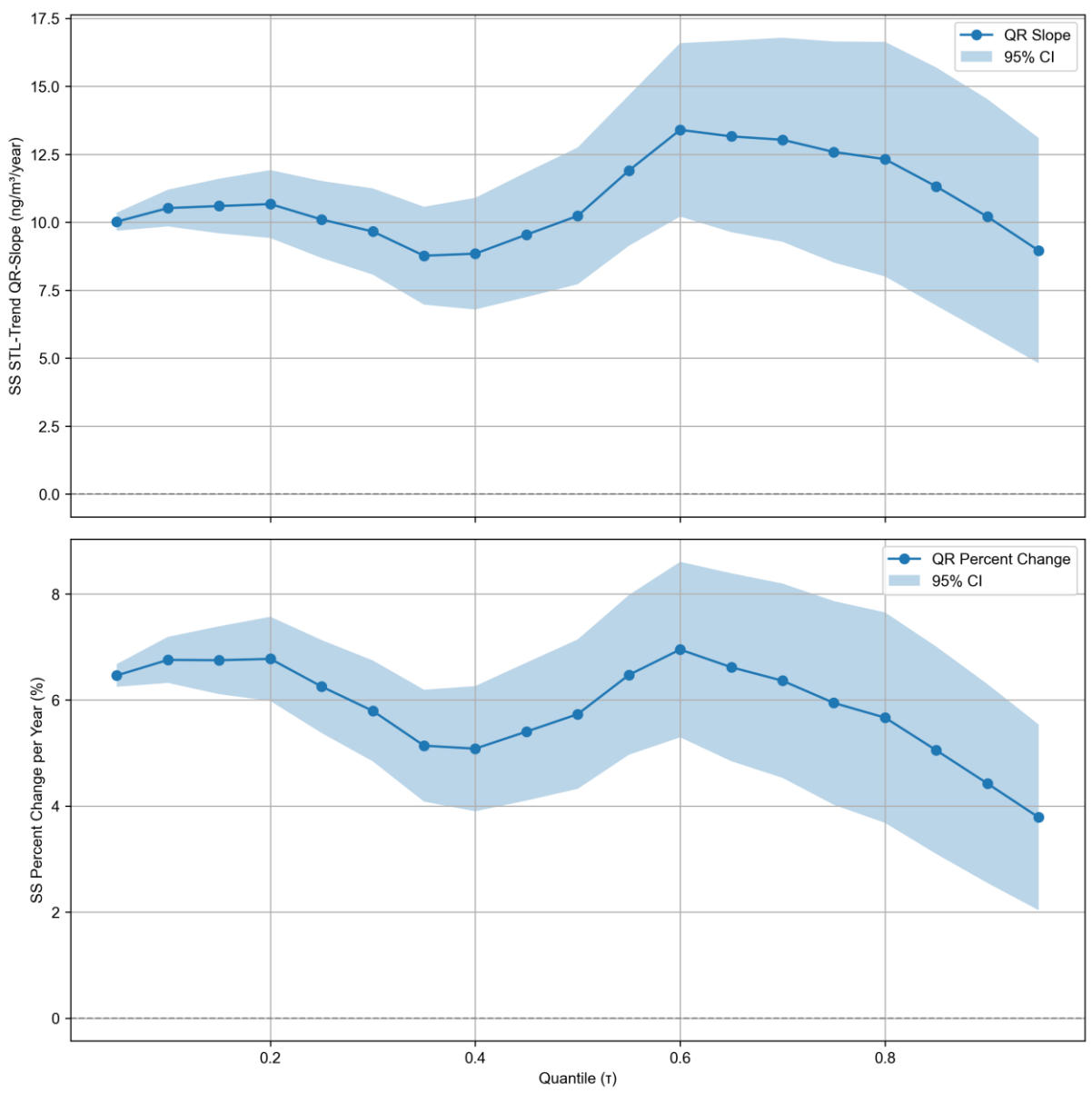
QR Slope
95% CI
SS STL-Trend QR-Slope (ng/m³/year)
17.5
15.0
12.5
10.0
7.5
5.0
2.5
0.0
QR Percent Change
95% CI
SS Percent Change per Year (%)
8
6
4
2
0
0.2
0.4
0.6
0.8
Quantile (τ)

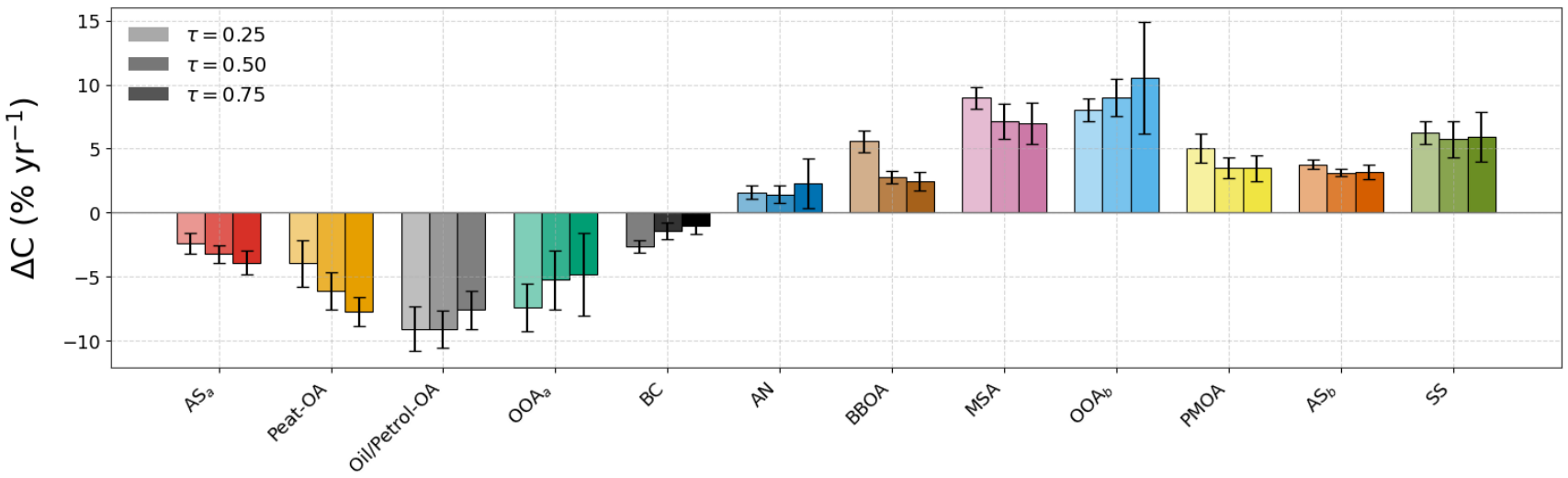

Figure S5. Same as Figure 3a but showing relative trends in mass concentration change (% yr^{-1}) for MHD aerosol components.

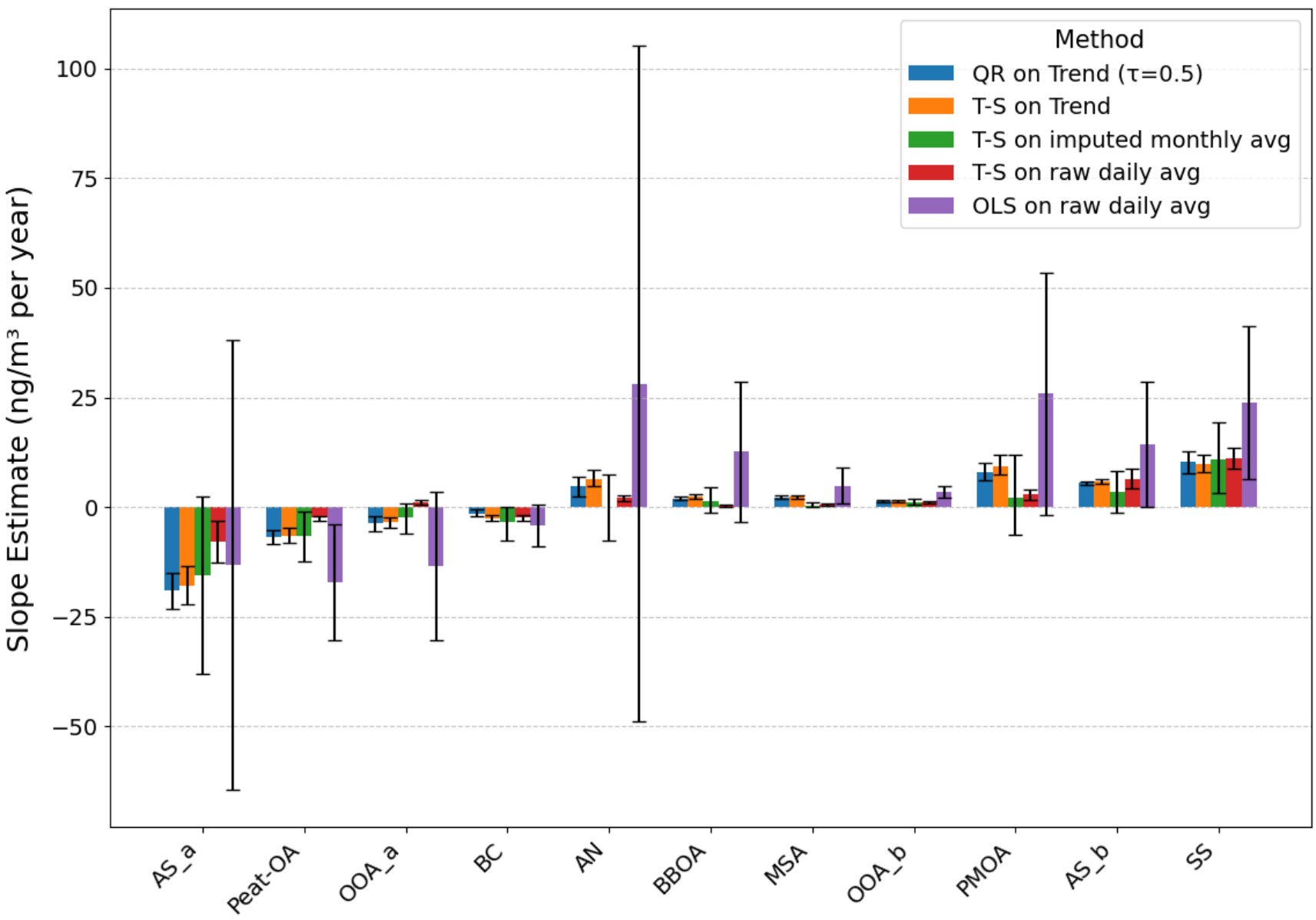

Figure S6. Comparison of median trend slope estimates across methods (QR at τ=0.5; Theil–Sen; OLS) applied to different preprocessing levels. QR and Theil–Sen applied to the same STL-Trend components (i.e. deseasonalized, low-frequency signal) provide the most direct comparison. Theil–Sen and OLS applied to imputed monthly means (without STL) or to raw daily means retain strong seasonality and serial dependence; these cases are therefore included as a sensitivity illustration of how aggregation and unremoved seasonal autocorrelation can widen uncertainty and alter slope magnitudes.

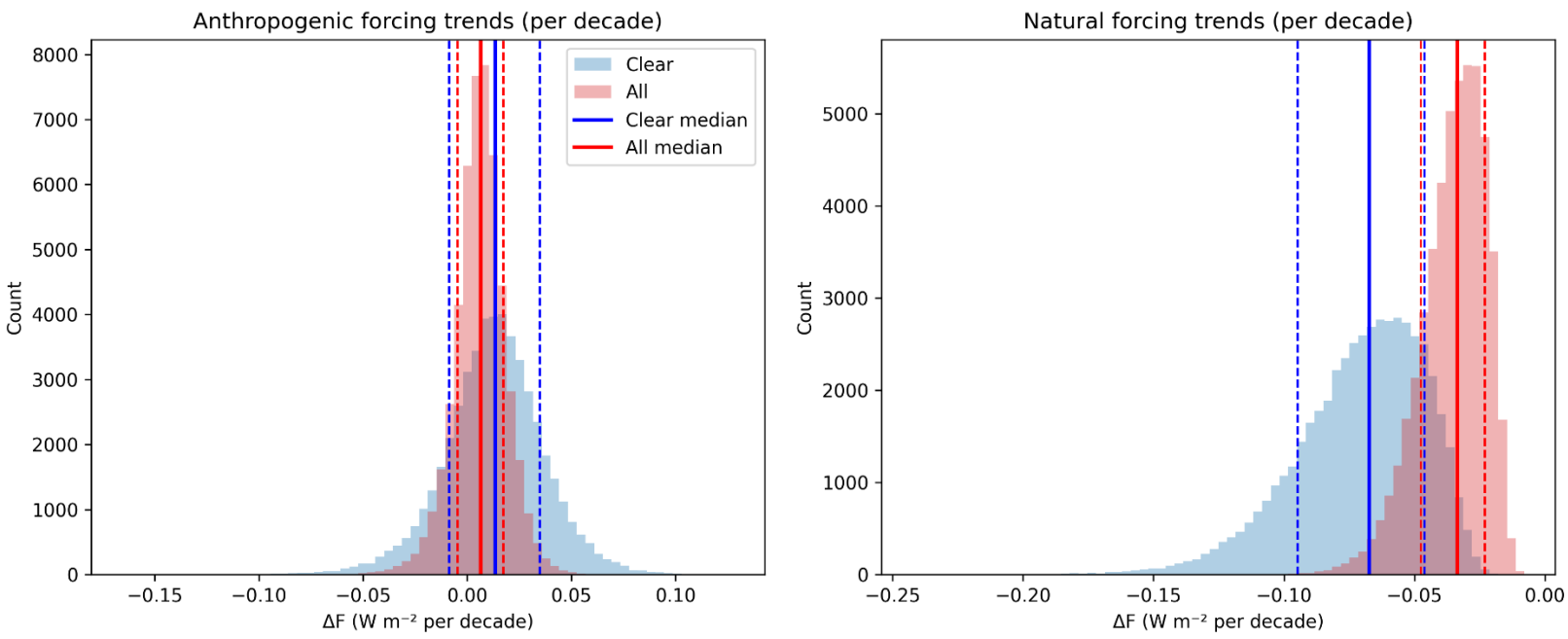

Figure S7. Probability distributions of radiative forcing trends (in W m^{-2} per decade) derived from Monte Carlo simulations for MHD, 2008–2019 (STL Trends, QR τ=0.50 case shown here). Shown are (a) anthropogenic components (combined), (b) natural components (combined), (c) and net forcing (anthropogenic + natural). Histograms represent clear-sky (blue; no clouds) and all-sky (red; mixed clear and cloudy) conditions (Text S4). Vertical solid lines indicate median values, while dashed lines denote the 16th & 84th percentiles (≈68% confidence interval).

SI Tables

Table S1. QR slope estimates at τ=0.95 (in ng m^{-3}) for STL Residuals of all aerosol components at MHD, along with ranges corresponding to 95% confidence intervals (CI). A positive or negative slope with a range that excludes zero indicates a statistically significant (SS) trend in extreme concentration events beyond the long-term and seasonal baseline.

Aerosol component	STL Residual Slope (τ=0.95)	Range	SS?
AS_a	1.5	[-76, 79]	no
Peat-OA	17.2	[-14, 48]	no
Oil/Petrol-OA	-13.2	[-41, 15]	no
OOA_a	-16.2	[-46, 13]	no
BC	-9.5	[-21, 2.5]	no
AN	96.8	[56.8, 137]	yes
BBOA	61.9	[4.7, 119]	yes
MSA	1.8	[-0.2, 3.8]	no
OOA_b	-0.9	[-3.4, 1.5]	no
PMOA	83.2	[13.3, 153]	yes
AS_b	7.5	[-31, 46]	no
SS	11.0	[-14.5, 36]	no

Table S2. Monte-Carlo parameter ranges (min, central, max) for component-specific direct radiative forcing calculations. For BC (coated; lensing effect considered), we sampled MAC instead of MEE and combined with SSA to split absorption/scattering. Values are central/nominal, without ±20% stochastic perturbation or all-sky scaling.

Component	$MEE_{550,dry}$ (m^2 g^{-1})	*α* (scat)	f(RH, ~85%)	AAE	SSA_{550}
AS	2.0 / 3.0 / 4.0	1.6 / 2.0 / 2.4	1.6 / 1.9 / 2.3	0.5 / 1.0 / 1.5	0.995 / 0.999 / 1.0
AN	2.0 / 3.0 / 4.0	1.6 / 2.0 / 2.4	1.6 / 1.9 / 2.3	0.5 / 1.0 / 1.5	0.995 / 0.999 / 1.0
SS	2.0 / 3.5 / 6.0	0.7 / 1.0 / 1.3	2.5 / 3.1 / 3.8	0.5 / 1.0 / 1.5	0.995 / 0.999 / 1.0
MSA	2.5 / 3.5 / 4.5	1.6 / 2.0 / 2.4	1.4 / 1.7 / 2.1	0.5 / 1.0 / 1.5	0.995 / 0.999 / 1.0
PMOA	2.5 / 3.5 / 4.5	1.6 / 2.0 / 2.4	1.2 / 1.4 / 1.7	0.7 / 1.0 / 1.5	0.98 / 0.99 / 1.0
OOA_b	2.5 / 3.5 / 4.5	1.6 / 2.0 / 2.4	1.3 / 1.6 / 1.9	0.8 / 1.0 / 1.3	0.98 / 0.995 / 1.0
OOA_a	3.0 / 4.0 / 5.0	1.6 / 2.0 / 2.4	1.2 / 1.4 / 1.7	1.5 / 2.0 / 2.5	0.94 / 0.97 / 0.99
BBOA	4.0 / 6.0 / 7.0	1.3 / 1.8 / 2.1	1.1 / 1.2 / 1.4	3.0 / 5.0 / 7.0	0.85 / 0.90 / 0.95
Peat-OA	3.5 / 5.0 / 6.0	1.3 / 1.8 / 2.1	1.1 / 1.2 / 1.4	3.0 / 4.0 / 5.0	0.88 / 0.92 / 0.96
Oil/Petrol-OA	2.5 / 3.0 / 4.0	1.2 / 1.3 / 1.4	1.1 / 1.15 / 1.3	1.0 / 1.5 / 2.0	0.97 / 0.98 / 0.995
BC	7 / 11 / 15 (MAC)	0.8 / 1.2 / 1.6	1.4 / 1.7 / 2.1	0.8 / 1.1 / 1.4	0.3 / 0.45 / 0.6

Supplementary Text

Text S1. HR-ToF-AMS Measurements and Processing

An Aerodyne high-resolution time-of-flight aerosol mass spectrometer (HR-ToF-AMS, Billerica, MA) has been operating at Mace Head since December 2008 to measure non-refractory PM_1 components. In AMS, particles flow in through an inlet and are focused with an aerodynamic lens into a detection chamber where they are flash vaporized on a hot oven and ionised by a beam of electrons. They can then be detected and chemically characterised using mass spectrometry. The instrument operated in single-reflection V-mode (mass resolution up to 3000 m/Δm), using a tungsten vaporizer at 650 °C until 2019. In 2021, the system was upgraded to a capture vaporizer, which introduces significant changes in aerosol particle flash vaporization efficiency and ionisation behaviour (particularly for semi-volatile organics), potentially affecting direct comparability with the earlier dataset.

To ensure methodological consistency and avoid artefacts in long-term trend estimation, we limited our analysis to the period 2008–2019. This interval offers a continuous, methodologically homogeneous dataset suitable for STL decomposition, which requires temporally consistent time series with minimal discontinuities (no data are available between May 2019 and April 2021 due to instrument downtime and subsequent hardware upgrades). Exclusion of recent data therefore avoids conflating instrumental shifts with true atmospheric trends, thereby reducing the risk of bias in the decomposition results. The selected decadal period is also sufficiently long to detect robust trends.[1]

We conducted high-resolution analysis of the 2008–2019 AMS data using SQUIRREL (SeQUential Igor data RetRiEvaL) v1.66G and PIKA (Peak Integration by Key Analysis) v1.26G in Igor Pro 9.02. For each tuning regime, we created separate Igor experiment files to reflect distinct ion optics and detector characteristics. We performed the HR analysis on each fitted *m/z* in the mass range 12–130 *m/z* with ion fitting applied to the difference between open and closed spectra. We discarded from further analysis data corresponding to background, particle-free air measurements, maintenance periods, and short-term campaigns or experiments.

We quantified MSA by upscaling the $CH_3SO_2^+$ fragment using a coefficient determined based on calibrations and compared with the time series of the AMS-PMF-derived MSA-OA factor. We corrected interference of MSA on HR-SO_4 using: $SO_{4,corr}$ = HR-SO_4 – (CH_3SO_2 * 12.48) / RIE_{SO4}. Non-sea-salt sulfate (nssSO_4) and sea-salt sulfate (ssSO_4) can both contribute to the corrected SO_4 concentrations; therefore, we evaluated the contribution of nssSO_4 by subtracting the ssSO_4 concentration (7.7% of sea-salt; see below)[2] from the total SO_4 concentration. We approximated the sea-salt (SS) mass concentration using the $^{23}Na^{35}Cl^+$ ion at *m/z* 57.96 and SS calibration scaling factors based on past comparisons with mono-disperse laboratory generated SS aerosol.[2] We corrected the particle transmission and detection efficiency, expressed as the collection efficiency, for detection losses due to particle bounce and lens efficiency, by applying the composition-dependent collection efficiency to nss non-refractory components.[3,4]

Text S2. PMF Setup/Evaluation and post-processing attribution

To characterise source contributions to OA, we applied positive matrix factorization (PMF) to the MHD HR-ToF-AMS OA mass spectra using the SoFi v6.8.1 toolkit. We first performed an unconstrained ("free") PMF on the year 2010 data at the native 10-min time resolution to establish a robust, physically interpretable factor set before extending the analysis to the full decadal record. Year 2010 was selected as the initial training/identification period because it provides a sufficiently long, continuous and well-populated dataset spanning multiple seasons and air-mass regimes. Running PMF at raw 10-min resolution maximises temporal variability and source contrasts, which improves separability of primary and secondary OA types and reduces the risk that short-lived events (e.g. episodic combustion plumes or rapid marine bursts) are smoothed out during factor identification. This "identify-first, extend-second" approach yields a stable set of reference factor profiles that can then be applied consistently across years.

Using free PMF on 2010 spectra, we identified six OA factors (Fig. S1): hydrocarbon-like OA from regional oil/petrol burning (Oil/Petrol-OA), peat-combustion OA (Peat-OA), biomass-burning OA (BBOA), primary marine OA (PMOA), methanesulfonic-acid-related OA (MSA-OA), and oxygenated OA (OOA). A solution with an additional (7th) factor was explored but was not physically interpretable and did not provide meaningful separation beyond the six-factor case. Factor validation was largely based on spectral matching (cosine similarity) against established factor profiles from previous work, including MHD/Ireland studies (see below).

After establishing and validating this six-factor set, we extended the analysis to the entire decadal dataset by averaging the HR OA mass spectra to hourly time resolution and performing a multi-year PMF analysis using the 2010-derived factors as constraints. The PMF input matrix consisted of the organic HR mass spectra time series (24–130 *m/z*), comprising 352 HR fragment ion intensities × 60,298 hourly samples, after pre-filtering for data-quality flags, blank/background periods, and campaign/maintenance intervals. We calculated each hourly uncertainty in the error matrix by combining the individual 10-min errors in quadrature and dividing by the number of points contributing to the hour. We then ran the SoFi PMF module with rotational parameter *a* = 0.1, allowing moderate flexibility in long-term factor variability while maintaining consistent factor identity across years.

The final constrained multi-year solution achieved $Q/Q_{exp} \approx 1.5$. The sum of the six OA factor masses strongly correlated with the PMF input (combined 352 HR fragments) OA mass for the decadal hourly samples (Pearson's *r* = 0.994), demonstrating excellent mass closure (slope = 0.953).

The calculated monthly MSA, by upscaling the $CH_3SO_2^+$ fragment (Text S1), strongly correlated with the AMS-PMF-based MSA-OA factor time series (slope: 0.99; Pearson's r: 0.93), and increased exponentially with solar irradiation (R^2 = 0.50); we used PVGIS (v5) geo-temporal irradiation fields to provide a spatially consistent estimate of downwelling solar irradiance representative of the broader upwind marine sector influencing MHD, rather than relying on point measurements at the station (for consistency with the MSA time series, irradiation was extracted using the MHD coordinates). The MSA-OA factor MS profile is similar (cosine similarity: 0.882) to that obtained by Chevassus et al. (2025) from summer 2015 MHD HR-AMS data.[5] The PMOA factor MS profile is highly similar (cosine similarity: 0.985) to that retrieved by Ovadnevaite et al. (2011) from August 2009 MHD HR-AMS data.[6] The Oil/Petrol-OA factor MS profile is highly similar (cosine similarity: 0.978) to the HOA factor MS profile reported by Crippa et al. (2011).[7] The BBOA factor MS profile is highly similar (cosine similarity: 0.964) to that reported by Lin et al. (2017)[8] from wood burning experiments in Ireland, when excluding *m/z* 44 from the comparison; because our BBOA profile has a consistent fingerprint with the controlled experiments producing primary wood-burning emissions[8] but has an elevated *m/z* 44 fragment intensity, we hypothesize that it largely represents aged biomass burning emissions that have been transported to MHD, from regional residential burning and/or gorse and grass fires.

BBOA represents a mixture of regional residential wood burning and wildfire emissions transported from surrounding uplands. Its classification with the natural/biogenic group reflects our focus on climate-sensitive biomass-burning processes and the strong association of upper-tail BBOA events with wildfire periods in western Ireland uplands but does not imply a purely natural origin. We therefore interpret our anthropogenic–natural split as "dominant influence" rather than a strict binary separation. In line with this, our radiative forcing conclusions are robust to reclassifying BBOA as anthropogenic, and key results and conclusions do not hinge on this categorical choice.

In contrast to BBOA, the aethalometer BC record at MHD predominantly reflects anthropogenic combustion. BC peaks in late winter/early spring together with AN, Peat-OA and Oil/Petrol-OA (Fig. 1) and declines across quantiles over the decade (Fig. 3, S4–S5) even as wildfire-linked BBOA extremes increase (Text S4). These features, combined with global assessments showing that the bulk of atmospheric BC arises from anthropogenic fossil-fuel and biofuel combustion,[9] support classifying BC entirely within the anthropogenic(-dominated) group. Practically, our BC series therefore captures BC from all combustion sources but is interpreted as "anthropogenic BC" in the sense used for short-lived climate forcers in IPCC and emission-inventory frameworks.

NH_4 is usually neutralised in higher-concentration continental air masses; we determined the mass concentration of ammonium-nitrate (AN; predominantly anthropogenic) and ammonium-sulfate (AS) salts (as needed for radiative forcing trend calculations; Text S4) by multiplying NO_3 by 1.291 and $nssSO_4$ by 1.376, respectively. The calculated biogenic ammonium-sulfate (AS_b) mass likely overestimates true marine biogenic nss-sulfate, as clean marine air masses typically have low ammonium levels and are often not fully neutralised (unlike continental air masses) resulting in acidic aerosols such as NH_4HSO_4 or even free H_2SO_4.

A tracer- and wind-sector–based threshold attribution (rule-based, fuzzy-scored) with Gaussian-kernel temporal smoothing for AS and OAA anthropogenic vs. natural contributions apportionment: To differentiate biogenic and anthropogenic contributions to AS and OOA, we applied a criteria-based attribution method based on both tracer concentrations and meteorological parameters. We classified hourly data as biogenic if wind direction was between 190–300° (marine sector) and markers of combustion were negligible, i.e. BC < 16.1 ng/m³, Peat-OA < 8.2 ng/m³, and Oil/Petrol-OA < 3.0 ng/m³; we determined these thresholds from the 25th percentile of the $\log_{10}$(mass concentration) histograms. We assigned a biogenic fraction (0–1) to each hourly data point based on how many of these conditions were met and used that to partition AS and OOA accordingly. We applied Gaussian smoothing (σ = 2 h) to the resulting time series to ensure realistic temporal transitions. We enforced mass closure such that the sum of marine biogenic and continental anthropogenic contributions equalled the original total for each component. Overall, this approach attributed 21% of AS and 15% of OOA to natural (marine biogenic) sources. While this approach effectively identifies westerly marine derived AS and OOA, it may overlook biogenic inputs from easterly air masses that traverse Ireland. As a result, the calculated anthropogenic contributions likely represent an upper limit, though they likely remain predominantly anthropogenic.

Text S3. Additional Information on STL & QR Analysis

STL Parameterisation and Justification: We applied Seasonal-Trend decomposition via Loess (STL) to monthly-averaged aerosol time series to extract trend, seasonal, and residual components. To minimise bias due to data gaps, we imputed missing monthly values (e.g. from partial instrument downtime) using the median of the corresponding calendar month across all available years. This conservative infilling preserves the observed climatological seasonal cycle and avoids extrapolating from short-term anomalies, at the cost of slightly damping intra-annual variability. We further applied a monthly completeness criterion whereby months with <25% available hourly data were classified as unreliable and also imputed. We chose this threshold (20% of the total months were imputed) to avoid a situation in which a stricter requirement would flag most months as incomplete, leading to extensive imputation and an undue influence of model-based values on the results, thereby increasing the risk of bias.

Besides the z-score-normalised climatological monthly profiles (Fig. 1), power spectral density analysis of the monthly time series confirmed a dominant frequency at ~0.083 month^{-1} across variables, indicating an expected annual periodicity (12 months) for anthropogenic and natural aerosol components. Therefore, to ensure consistency across variables and avoid overfitting, we configured STL with a fixed periodicity of 12 months to reflect the annual cycle in the seasonal components. Further, we set the seasonal smoothing parameter value to 7 to balance fidelity to short-term seasonal variability and suppression of high-frequency noise, while also allowing for the seasonal amplitude to vary between years (as opposed to a fixed periodic setting). We set the trend smoothing parameter to 23, derived from a Cleveland et al. (1990)[10] empirical formula suggesting to set *trend_window* to the smallest odd integer exceeding *1.5×period / [1−1.5/seasonal_window]*, where in our case period=12 and seasonal_window=7, as explained above. This parameter combination ensures clear separation between seasonal and trend components and avoids allocation of intermediate-frequency variance to the residual term. We executed STL with robust fitting enabled, down-weighting outliers such as those caused by extreme pollution events.

Diagnostics of STL Residuals: To assess the suitability of STL decomposition and identify any remaining temporal structure in the STL-Residuals before upper-quantile analysis (τ=0.95), we applied the Ljung–Box test for autocorrelation across lags up to 24 months. Residual autocorrelation can persist when STL does not fully remove low-frequency variability (e.g. slowly evolving meteorology or emission regime shifts), and if left uncorrected it violates the independence assumption and can bias uncertainty and significance in subsequent quantile-based inference. Where residual autocorrelation was statistically significant ($p < 0.05$), we fitted autoregressive (AR) models to account for serial dependence. we tested AR(1) first; if inadequate, we selected the optimal AR(p) model (p = 1–10) using the minimum Akaike Information Criterion.

Quantile Regression Methodology: We applied QR to the STL-derived Trend and Residual components to estimate trends across different parts of the distribution (τ=0.05 to 0.95, in 0.05 increments). This allows for identification of asymmetric changes in background levels (lower quantiles), central tendency (median), and extremes (upper quantiles). The method is particularly well-suited for atmospheric pollutant data, which often exhibit skewed and heavy-tailed distributions. We computed QR slopes using the *statsmodels* implementation in Python, and calculated confidence intervals (95%) using a heteroskedasticity- and autocorrelation-consistent covariance estimator.

QR of Residuals and Extreme Events: We applied quantile regression on STL Residuals at τ=0.95 to quantify the temporal evolution of extreme pollution events, i.e. those that exceed expected seasonal and trend behaviour. This method isolates high-end deviations and enables identification of changing intensity or frequency of episodic pollution spikes, particularly relevant for naturally driven components such as wildfire-related OA or marine biogenic aerosol. The statistical significance and magnitude of residual trends at τ=0.95 are provided in Table S1.

Text S4. Additional Information on Radiative Forcing Calculations

From concentration trends to column burdens: We converted surface concentration trends to column burden trends assuming surface observations are representative of the mixed marine boundary layer. We therefore treat *H* as an effective mixed-layer depth to translate near-surface mass trends to vertically integrated burdens. The component-specific (*i*) incremental change in vertically integrated burden (ΔB_i, g m^{-2} yr^{-1}) is: $\Delta B_i = \Delta C_i \cdot H \cdot 10^{-9}$

where ΔC is the concentration trend (ng m^{-3} yr^{-1}), H is the mixed layer depth (m), and 10^{-9} converts ng to g. Boundary-layer depth was drawn uniformly from 500–1200 m, consistent with northeast Atlantic climatology.[11,12]

Conversion to aerosol optical depth: We converted burden changes to aerosol optical depth increments (ΔAOD) using effective, relative humidity (RH)- and wavelength-dependent mass extinction efficiencies (MEE, m^2 g^{-1}) or mass absorption coefficients (MAC for BC): $\Delta AOD_i = \Delta B_i \cdot E_i$, where E_i is the spectrally integrated, humidified extinction efficiency for component *i*.

Direct radiative forcing efficiency: For each realization and each component *i*, we parameterised the clear-sky top-of-atmosphere forcing efficiency ε_i (W m^{-2} per unit AOD_{550}) as a function of its single-scattering albedo at 550 nm (SSA_i). First, we sampled a "purely scattering" endpoint ε_scat from a triangular distribution spanning −60, −50, and −40 W m^{-2} AOD^{-1}, corresponding to sulfate- and sea-salt-dominated marine aerosol,[13,14] to represent a bounded literature range with a most-likely value at the midpoint. We then sampled an absorbing black-carbon endpoint ε_abs from +70, +110, and +160 W m^{-2} AOD^{-19} and a BC SSA from 0.3–0.6 (Table S2). We obtained $\varepsilon_i(SSA_i)$ by interpolating between these two physically bounded endpoints in SSA space, such that ε_scat applies at SSA = 1 and ε_abs applies at the sampled BC SSA. An additional ±20% Gaussian perturbation was applied to account for unresolved variability in viewing geometry and surface albedo.

Monte Carlo uncertainty propagation: We performed 50,000 Monte Carlo simulations to propagate uncertainties in ΔC_i, H, extinction efficiency (E_i), and forcing efficiency (ε). For each realization:

- **ΔC (ng m^{-3} yr^{-1})**: sampled from a normal distribution centered on the QR slope estimate, with the standard deviation taken as half the width of the QR confidence interval.
- **Column height (H):** drawn from a uniform distribution between 500–1200 m.
- **Extinction efficiency (E_i)** and spectral weighting: for each component *i*, we split 550 nm extinction into scattering and absorption, apply RH growth to the scattering part only, and then computed a spectrally weighted broadband extinction efficiency, E_i (m^2 g^{-1}). Scattering and absorption cross-sections were extrapolated from 550 nm using the scattering Ångström exponent (α) and absorption Ångström exponent (AAE), respectively. The resulting spectra were integrated from 300 nm to the end of the shortwave band using the ASTM G173-03 AM1.5G global-tilt reference spectrum as a wavelength-dependent weighting function. Thus, E_i represents a humidified, broadband shortwave extinction efficiency that is consistent with the solar spectrum at the surface. We sampled E_i from component-specific ranges (Table S2):
  - **MEE (dry, 550 nm):** 2.0–4.0 for AS/AN,[15] 2.5–5 for OOA,[16] 2.5–4.5 for PMOA,[15] 2.0–6.0 for submicron SS[15,17] 4–7 for BBOA, 3.5–6 for Peat OA, 2.5–4 for Oil/Petrol OA. Compared with non-absorbing OAs, we assigned higher typical MEEs to light-absorbing anthropogenic OA (brown-carbon-containing) components (BBOA>Peat-OA>OOA>Oil/Petrol_OA), due to their non-negligible absorption in addition to scattering.[18-21] MEE denotes *mass extinction efficiency* (scattering + absorption). Component extinction is partitioned into scattering and absorption using the sampled SSA_{550}, i.e. σ_scat = SSA·σ_ext and σ_abs = (1−SSA)·σ_ext.
  - **MAC for BC** (coated, 550 nm)**:** 7–15 m^2 g^{-1};[22,23] σ_abs is derived from MAC and σ_scat is represented implicitly via SSA_{550}.
  - ***f*(RH) (scattering enhancement at ~85% RH)**[11,24-31]**:** 1.6–2.3 for inorganics, 1.1–1.9 for OA (higher for biogenic oxygenated OA), 2.5–3.8 for SS, 1.4–2.1 for coated BC.
  - **Scattering Ångström exponent (α)**[32-34]**:** 1.6–2.4 for AS, AN, OOA, PMOA, 0.7–1.3 for SS, 1.3–2.1 for BBOA and Peat-OA, 1.2–1.4 for fossil OA, 0.8–1.6 for BC.
  - **Absorption Ångström exponent (AAE):** 0.8-1.4 for BC,[22,35-37] 1–2 for fossil OA, 1.5–2.5 for anthropogenic OOA, 3–7 for BBOA,[38] 3–5 for Peat-OA.[39] For nominally non-absorbing components (AS, AN, SS, MSA), absorption is constrained to be negligible via $SSA_{550} \approx 1$; the listed AAE values (Table S2) were therefore not used to create significant absorption but only provide a numerically consistent spectral extrapolation should any residual absorption arise.
  - **SSA (550 nm)**[40,41]**: ~**1.0 for inorganics/marine OA,[42] 0.85–0.95 for BBOA,[38] 0.88–0.96 for Peat-OA,[43] 0.97–0.995 for fossil OA,[44,45] 0.94–1.0 for OOA,[44,45] and 0.3–0.6 for BC.[9]
- **Forcing efficiency (ε_i):** calculated from SSA, α, and *f*(RH), with random variability (±20%).
  - ε_scat (clear-sky base): sampled from –40 to –60 W m^{-2} AOD^{-1} (mode –50).[46-52]
  - ε_abs (clear-sky base): sampled from +70 to +160 W m^{-2} AOD^{-1} (mode +110).[9,52]
- **Sky condition adjustment**: all-sky scaling = 0.5 × clear-sky efficiency (range: 0.4 to 0.6) to represent cloud masking.

All optical component-level ranges used here (MEE, α, *f*(RH), AAE, SSA) are based on size-resolved optical measurements at Mace Head and similar sites and are summarized in Table S2; thus, size-dependency of extinction and absorption is implicitly represented through these parameter distributions, i.e. we sampled a physically realistic size-dependent optical envelope. We used triangular distributions for optical parameters (E, ε), where we considered a minimum, most-likely (central), and maximum value from literature/site climatology. This clusters values around the most likely but allows excursions across the full plausible range. In the absence of strong constraints on covariance among these parameters, each was sampled within its literature-based uncertainty range as described above, so that the ensemble spans a plausible set of combinations of column burdens, optical properties, and forcing efficiencies consistent with prior knowledge.

Throughout the direct RF calculations, inorganic aerosol was represented as ammonium-sulfate (AS) and ammonium-nitrate (AN), derived from AMS measured $nssSO_4$ and NO_3, because published optical and hygroscopic parameterisations are defined for these salts rather than for individual ions, and this avoids double-counting co-located SO_4 and NH_4 mass in the same particles.

Aggregation and counterbalancing: For each realization: $\Delta F_i = \Delta C_i \cdot H \cdot 10^{-9} \cdot E_i \cdot \varepsilon_i$ (units: ng m^{-3} yr^{-1} · m · 10^{-9} → g m^{-2} yr^{-1}; multiplied by m^2 g^{-1} → AOD yr^{-1}; multiplied by W m^{-2} AOD^{-1} → W m^{-2} yr^{-1}).

We calculated group totals for anthropogenic vs. natural components:

$\Delta F_{anthro} = \sum_{i \in anthro} \Delta F_i$; $\Delta F_{nat} = \sum_{i \in nat} \Delta F_i$; $\Delta F_{net} = \Delta F_{anthro} + \Delta F_{nat}$

Results are reported as the median and 16th–84th percentiles of the Monte Carlo ensemble and annual forcing trends are expressed as W m^{-2} per decade. This treatment is consistent with major assessments (e.g. IPCC), where RF uncertainty is reported as probability ranges from ensemble or Monte Carlo approaches rather than as formal confidence intervals derived from statistical trend estimation.

Text S5. Assumptions and Limitations

Trend Analysis: While the timeseries used in this study (12 years) is robust for detecting long-term trends,[1] it is the well below the conventional threshold for climate timescales (30 years). The length of the time series can influence the analysis outcome therefore the conclusions of this study are limited to recent decades. The time series not starting and ending with complete calendar years may also add uncertainty.[1] Intra-annual variability can have an effect on the outcome of a trend analysis, especially for natural aerosol components, when dealing with a short time series.[53] The STL method accounts for this by incorporating anomalous values into the residual component. Thus, the Trend component only considers low frequency changes and allows for robust trends to be estimated. The STL method requires a complete time series as input data, therefore an imputation method needs to be implemented due to missing data. While this may introduce some uncertainty, the imputation method employed in this study (median of the corresponding calendar month across all available years) provides a robust estimate that preserves seasonal cycles and levels and is considered favourable over a simple mean or median imputer. Imputation would mainly affect the upper and lower quantiles, as imputed values would be similar to the average. Other methods, which rely on exogenous variables, such as k-nearest neighbours, principal component analysis, or predictive mean matching, could be explored for future analysis.

Discussion of ERF_{aci} Effects: This study focuses on direct radiative forcing (DRF), excluding aerosol–cloud interactions (ERF_{aci}). However, the latter typically dominates total aerosol forcing.[13] Global assessments suggest that ERF_{aci} is ~3–5× larger than DRF for sulfate and can range from −0.5 to −1.5 W m^{-2} globally. If similar ratios apply to our marine biogenic sulfate increases, the total negative forcing trend associated with natural aerosols may exceed –0.2 W m^{-2} per decade. However, ERF_{aci} exhibits larger spatial and seasonal variability and is more challenging to constrain observationally.[14] Quantifying its contribution with sufficient fidelity remains a key priority for model development and future measurement campaigns.

Uncertainty in Monte Carlo Simulations: An important assumption in our Monte Carlo analysis is that extinction efficiency (E_i), single scattering albedo (SSA), RH dependence (f(RH)), and other optical parameters are sampled independently. These properties are often correlated (e.g. hygroscopic growth simultaneously increases extinction and modifies scattering phase function and absorption properties). Ignoring such covariance may either over- or underestimate the effective uncertainty in forcing distributions. Because most empirical studies report only separate (univariate) parameter ranges rather than their co-variation, we sample each parameter independently to span a realistic range of variability, but we cannot fully represent co-dependent uncertainties between optical properties.

Uncertainty ranges reported for RF trends differ conceptually from the CIs shown for concentration trends. For aerosol mass concentrations, 95% CIs quantify the statistical uncertainty of QR slope estimates and are used to assess whether trends are statistically distinguishable from zero. In contrast, RF trends are derived from Monte Carlo propagation of physically based uncertainties in concentration trends, boundary-layer depth, optical properties, and forcing efficiencies. The resulting distributions therefore represent probabilistic uncertainty ranges rather than statistical confidence intervals on a fitted parameter. For RF, we report the median and 16th–84th percentiles (≈1 standard deviation) of the Monte Carlo ensemble. This range captures the central, most probable spread of physically plausible forcing outcomes and facilitates comparison across components and sites. It is not intended to define statistical significance, and zero-crossing of this range should not be interpreted in the same manner as confidence-interval-based significance testing applied to concentration trends.

SI References

[1] Collaud Coen, M.; Andrews, E.; Bigi, A.; Martucci, G.; Romanens, G.; Vogt, F. P. A.; Vuilleumier, L. Effects of the prewhitening method, the time granularity, and the time segmentation on the Mann–Kendall trend detection and the associated Sen's slope. *AMT* **2020**, *13* (12), 6945-6964. DOI: 10.5194/amt-13-6945-2020.

[2] Ovadnevaite, J.; Ceburnis, D.; Canagaratna, M.; Berresheim, H.; Bialek, J.; Martucci, G.; Worsnop, D. R.; O'Dowd, C. On the effect of wind speed on submicron sea salt mass concentrations and source fluxes. *JGR Atmos.* **2012**, *117*. Artn D16201, DOI: 10.1029/2011jd017379.

[3] Ovadnevaite, J.; Ceburnis, D.; Leinert, S.; Dall'Osto, M.; Canagaratna, M.; O'Doherty, S.; Berresheim, H.; O'Dowd, C. Submicron NE Atlantic marine aerosol chemical composition and abundance: Seasonal trends and air mass categorization. *JGR Atmos.* **2014**, *119* (20), 11,850-811,863. DOI: 10.1002/2013jd021330.

[4] Middlebrook, A. M.; Bahreini, R.; Jimenez, J. L.; Canagaratna, M. R. Evaluation of Composition-dependent collection efficiencies for the Aerodyne aerosol mass spectrometer using field data. *Aerosol Sci. Tech.* **2012**, *46* (3), 258-271. DOI: 10.1080/02786826.2011.620041.

[5] Chevassus, E.; Fossum, K. N.; Ceburnis, D.; Lei, L.; Lin, C.; Xu, W.; O'Dowd, C.; Ovadnevaite, J. Marine organic aerosol at Mace Head: effects from phytoplankton and source region variability. *ACP* **2025**, *25* (7), 4107-4129. DOI: 10.5194/acp-25-4107-2025.

[6] Ovadnevaite, J.; O'Dowd, C.; Dall'Osto, M.; Ceburnis, D.; Worsnop, D. R.; Berresheim, H. Detecting high contributions of primary organic matter to marine aerosol: A case study. *GRL* **2011**, *38*. Artn L02807, DOI: 10.1029/2010gl046083.

[7] Crippa, M.; DeCarlo, P. F.; Slowik, J. G.; Mohr, C.; Heringa, M. F.; Chirico, R.; Poulain, L.; Freutel, F.; Sciare, J.; Cozic, J.; et al. Wintertime aerosol chemical composition and source apportionment of the organic fraction in the metropolitan area of Paris. *ACP* **2013**, *13* (2), 961-981. DOI: 10.5194/acp-13-961-2013.

[8] Lin, C. S.; Ceburnis, D.; Hellebust, S.; Buckley, P.; Wenger, J.; Canonaco, F.; Prévôt, A. S. H.; Huang, R. J.; O'Dowd, C.; Ovadnevaite, J. Characterization of Primary organic aerosol from domestic wood, peat, and coal burning in Ireland. *Environ. Sci. Technol.* **2017**, *51* (18), 10624-10632. DOI: 10.1021/acs.est.7b01926.

[9] Bond, T. C.; Doherty, S. J.; Fahey, D. W.; Forster, P. M.; Berntsen, T.; DeAngelo, B. J.; Flanner, M. G.; Ghan, S.; Kärcher, B.; Koch, D.; et al. Bounding the role of black carbon in the climate system: A scientific assessment. *JGR Atmos.* **2013**, *118* (11), 5380-5552. DOI: 10.1002/jgrd.50171.

[10] Cleveland, R.B., Cleveland, W.S. STL: A Seasonal-Trend Decomposition procedure based on Loess. *J. Off. Stat.* **1990**, 6, 3-33.

[11] Dall'Osto, M.; Ceburnis, D.; Martucci, G.; Bialek, J.; Dupuy, R.; Jennings, S. G.; Berresheim, H.; Wenger, J.; Healy, R.; et al. Aerosol properties associated with air masses arriving into the North East Atlantic during the 2008 Mace Head EUCAARI intensive observing period: An overview. *ACP* **2010**, *10* (17), 8413-8435. DOI: 10.5194/acp-10-8413-2010.

[12] Kirschler, S.; Voigt, C.; Anderson, B. E.; Chen, G.; Crosbie, E. C.; Ferrare, R. A.; Hahn, V.; Hair, J. W.; Kaufmann, S.; Moore, R. H.; et al. Overview and statistical analysis of boundary layer clouds and precipitation over the western North Atlantic Ocean. *ACP* **2023**, *23* (18), 10731-10750. DOI: 10.5194/acp-23-10731-2023.

[13] IPCC, 2021: Climate Change 2021: The Physical Science Basis. Contribution of Working Group I to the 6th Assessment Report of the Intergovernmental Panel on Climate Change [Masson-Delmotte, V., P. Zhai, A. Pirani, S.L. Connors, C.

[14] Bellouin, N.; Quaas, J.; Gryspeerdt, E.; Kinne, S.; Stier, P.; Watson-Parris, D.; Boucher, O.; Carslaw, K. S.; Christensen, M.; Daniau, A. L.; et al. Bounding global aerosol radiative forcing of climate change. *Rev. Geophys.* **2020**, *58* (1). ARTN e2019RG000660, DOI: 10.1029/2019RG000660.

[15] Hand, J. L.; Malm, W. C. Review of aerosol mass scattering efficiencies from ground-based measurements since 1990. *J Geophys Res-Atmos* **2007**, *112* (D18). Artn D16203, DOI: 10.1029/2007jd008484.

[16] Latimer, R. N. C.; Martin, R. V. Interpretation of measured aerosol mass scattering efficiency over North America using a chemical transport model. *ACP* **2019**, *19* (4), 2635-2653. DOI: 10.5194/acp-19-2635-2019.

[17] Jaeglé, L.; Quinn, P. K.; Bates, T. S.; Alexander, B.; Lin, J. T. Global distribution of sea salt aerosols: new constraints from in situ and remote sensing observations. *ACP* **2011**, *11* (7), 3137-3157. DOI: 10.5194/acp-11-3137-2011.

[18] Andreae, M. O.; Gelencsér, A. Black carbon or brown carbon?: The nature of light-absorbing carbonaceous aerosols. *ACP* **2006**, *6*, 3131-3148. DOI: DOI 10.5194/acp-6-3131-2006.

[19] Saleh, R.; Robinson, E. S.; Tkacik, D. S.; Ahern, A. T.; Liu, S.; Aiken, A. C.; Sullivan, R. C.; Presto, A. A.; Dubey, M. K.; Yokelson, R. J.; et al. Brownness of organics in aerosols from biomass burning linked to their black carbon content. *Nat. Geosci.* **2014**, *7* (9), 647-650. DOI: 10.1038/Ngeo2220.

[20] Moschos, V.; Kumar, N. K.; Daellenbach, K. R.; Baltensperger, U.; Prévôt, A. S. H.; El Haddad, I. Source apportionment of brown carbon absorption by coupling ultraviolet-visible spectroscopy with aerosol mass spectrometry. *Environ. Sci. Technol. Lett.* **2018**, *5* (6), 302-+. DOI: 10.1021/acs.estlett.8b00118.

[21] Moschos, V.; Gysel-Beer, M.; Modini, R. L.; Corbin, J. C.; Massabò, D.; Costa, C.; Danelli, S. G.; Vlachou, A.; Daellenbach, K. R.; Szidat, S.; et al. Source-specific light absorption by carbonaceous components in the complex aerosol matrix from yearly filter-based measurements. *ACP* **2021**, *21* (16), 12809-12833. DOI: 10.5194/acp-21-12809-2021.

[22] Bond, T. C.; Bergstrom, R. W. Light absorption by carbonaceous particles: An investigative review. *Aerosol Sci. Tech.* **2006**, *40* (1), 27-67. DOI: 10.1080/02786820500421521.

[23] Zhao, W. L.; Tan, W. S.; Zhao, G.; Shen, C. Y.; Yu, Y. L.; Zhao, C. S. Determination of equivalent black carbon mass concentration from aerosol light absorption using variable mass absorption cross section. *AMT* **2021**, *14* (2), 1319-1331. DOI: 10.5194/amt-14-1319-2021.

[24] Zieger, P.; Fierz-Schmidhauser, R.; Weingartner, E.; Baltensperger, U. Effects of relative humidity on aerosol light scattering: results from different European sites. *ACP* **2013**, *13* (21), 10609-10631. DOI: 10.5194/acp-13-10609-2013.

[25] Titos, G.; Cazorla, A.; Zieger, P.; Andrews, E.; Lyamani, H.; Granados-Muñoz, M. J.; Olmo, F. J.; Alados-Arboledas, L. Effect of hygroscopic growth on the aerosol light-scattering coefficient: A review of measurements, techniques and error sources. *Atmos. Environ.* **2016**, *141*, 494-507. DOI: 10.1016/j.atmosenv.2016.07.021.

[26] Titos, G.; Lyamani, H.; Cazorla, A.; Sorribas, M.; Foyo-Moreno, I.; Wiedensohler, A.; Alados-Arboledas, L. Study of the relative humidity dependence of aerosol light-scattering in southern Spain. *Tellus B* **2014**, *66*. ARTN 24536, DOI: 10.3402/tellusb.v66.24536.

[27] Jefferson, A.; Hageman, D.; Morrow, H.; Mei, F.; Watson, T. Seven years of aerosol scattering hygroscopic growth measurements from SGP: Factors influencing water uptake. *JGR Atmos.* **2017**, *122* (17), 9451-9466. DOI: 10.1002/2017jd026804.

[28] Vaishya, A.; Ovadnevaite, J.; Bialek, J.; Jennings, S. G.; Ceburnis, D.; O'Dowd, C. D. Bistable effect of organic enrichment on sea spray radiative properties. *GRL* **2013**, *40* (24), 6395-6398. DOI: 10.1002/2013gl058452.

[29] Fierz-Schmidhauser, R.; Zieger, P.; Vaishya, A.; Monahan, C.; Bialek, J.; O'Dowd, C. D.; Jennings, S. G.; Baltensperger, U.; Weingartner, E. Light scattering enhancement factors in the marine boundary layer (Mace Head, Ireland). *JGR Atmos.* **2010**, *115*. Artn D20204, DOI: 10.1029/2009jd013755.

[30] Burgos, M. A.; Andrews, E.; Titos, G.; Benedetti, A.; Bian, H. S.; Buchard, V.; Curci, G.; Kipling, Z.; Kirkevåg, A.; Kokkola, H.; et al. A global model-measurement evaluation of particle light scattering coefficients at elevated relative humidity. *ACP* **2020**, *20* (17), 10231-10258. DOI: 10.5194/acp-20-10231-2020.

[31] Virkkula, A.; Backman, J.; Aalto, P. P.; Hulkkonen, M.; Riuttanen, L.; Nieminen, T.; dal Maso, M.; Sogacheva, L.; de Leeuw, G.; Kulmala, M. Seasonal cycle, size dependencies, and source analyses of aerosol optical properties at the SMEAR II measurement station in Hyytiala, Finland. *ACP* **2011**, *11* (9), 4445-4468. DOI: 10.5194/acp-11-4445-2011.

[32] Ren, R. M.; Li, Z. Q.; Yan, P.; Wang, Y. Y.; Wu, H.; Cribb, M.; Wang, W.; Jin, X. A.; Li, Y. A.; Zhang, D. M. Measurement report: The effect of aerosol chemical composition on light scattering due to the hygroscopic swelling effect. *ACP* **2021**, *21* (13), 9977-9994. DOI: 10.5194/acp-21-9977-2021.

[33] Clarke, A.; Kapustin, V.; Howell, S.; Moore, K.; Lienert, B.; Masonis, S.; Anderson, T.; Covert, D. Sea-salt size distributions from breaking waves: Implications for marine aerosol production and optical extinction measurements during SEAS. *J. Atmos. Ocean. Tech.* **2003**, *20* (10), 1362-1374. DOI: Doi 10.1175/1520-0426(2003)020<1362:Ssdfbw>2.0.Co;2.

[34] Mulcahy, J. P.; O'Dowd, C. D.; Jennings, S. G. Aerosol optical depth in clean marine and continental northeast Atlantic air. *JGR Atmos.* **2009**, *114*. Artn D20204, DOI: 10.1029/2009jd011992.

[35] Zangmeister, C. D.; You, R.; Lunny, E. M.; Jacobson, A. E.; Okumura, M.; Zachariah, M. R.; Radney, J. G. Measured mass absorption spectra for nine forms of highly-absorbing carbonaceous aerosol. *Carbon* **2018**, *136*, 85-93. DOI: 10.1016/j.carbon.2018.04.057.

[36] Lack, D. A.; Cappa, C. D. Impact of brown and clear carbon on light absorption enhancement, single scatter albedo and absorption wavelength dependence of black carbon. *ACP* **2010**, *10* (9), 4207-4220. DOI: 10.5194/acp-10-4207-2010.

[37] Liu, C.; Chung, C. E.; Yin, Y.; Schnaiter, M. The absorption Angstrom exponent of black carbon: from numerical aspects. *ACP* **2018**, *18* (9), 6259-6273. DOI: 10.5194/acp-18-6259-2018.

[38] Pokhrel, R. P.; Wagner, N. L.; Langridge, J. M.; Lack, D. A.; Jayarathne, T.; Stone, E. A.; Stockwell, C. E.; Yokelson, R. J.; Murphy, S. M. Parameterization of single-scattering albedo (SSA) and absorption Angstrom exponent (AAE) with EC / OC for aerosol emissions from biomass burning. *ACP* **2016**, *16* (15), 9549-9561. DOI: 10.5194/acp-16-9549-2016.

[39] Popovicheva, O. B.; Engling, G.; Ku, I. T.; Timofeev, M. A.; Shonija, N. K. Aerosol emissions from long-lasting smoldering of boreal peatlands: Chemical composition, markers, and microstructure. *AAQR* **2019**, *19* (3), 484-503. DOI: 10.4209/aaqr.2018.08.0302.

[40] Jennings, S. G.; Kleefeld, C.; O'Dowd, C. D.; Junker, C.; Spain, T. G.; O'Brien, P.; Roddy, A. F.; O'Connor, T. C. Mace Head atmospheric research station characterization of aerosol radiative parameters. *Boreal Environ. Res.* **2003**, *8* (4), 303-314.

[41] Dubovik, O.; Holben, B.; Eck, T. F.; Smirnov, A.; Kaufman, Y. J.; King, M. D.; Tanré, D.; Slutsker, I. Variability of absorption and optical properties of key aerosol types observed in worldwide locations. *J. Atmos. Sci.* **2002**, *59* (3), 590-608.

[42] Bates, T. S.; Quinn, P. K.; Coffman, D. J.; Johnson, J. E.; Middlebrook, A. M. Dominance of organic aerosols in the marine boundary layer over the Gulf of Maine during NEAQS 2002 and their role in aerosol light scattering - art. no. D18202. *JGR Atmos.* **2005**, *110* (D18). Artn D18202, DOI: 10.1029/2005jd005797.

[43] Chand, D.; Schmid, O.; Gwaze, P.; Parmar, R. S.; Helas, G.; Zeromskiene, K.; Wiedensohler, A.; Massling, A.; Andreae, M. O. Laboratory measurements of smoke optical properties from the burning of Indonesian peat and other types of biomass. *GRL* **2005**, *32* (12). Artn L12819, DOI: 10.1029/2005gl022678.

[44] Dingle, J. H.; Zimmerman, S.; Frie, A. L.; Min, J.; Jung, H. J.; Bahreini, R. Complex refractive index, single scattering albedo, and mass absorption coefficient of secondary organic aerosols generated from oxidation of biogenic and anthropogenic precursors. *Aerosol Sci. Tech.* **2019**, *53* (4), 449-463. DOI: 10.1080/02786826.2019.1571680.

[45] Lacagnina, C.; Hasekamp, O. P.; Bian, H. S.; Curci, G.; Myhre, G.; van Noije, T.; Schulz, M.; Skeie, R. B.; Takemura, T.; Zhang, K. Aerosol single-scattering albedo over the global oceans: Comparing PARASOL retrievals with AERONET, OMI, and AeroCom models estimates. *JGR Atmos.* **2015**, *120* (18), 9814-9836. DOI: 10.1002/2015jd023501.

[46] Elsey, J.; Bellouin, N.; Ryder, C. Sensitivity of global direct aerosol shortwave radiative forcing to uncertainties in aerosol optical properties. *ACP* **2024**, *24* (7), 4065-4081. DOI: 10.5194/acp-24-4065-2024.

[47] Bellouin, N.; Quaas, J.; Morcrette, J. J.; Boucher, O. Estimates of aerosol radiative forcing from the MACC re-analysis. *ACP* **2013**, *13* (4), 2045-2062. DOI: 10.5194/acp-13-2045-2013.

[48] Meywerk, J.; Ramanathan, V. Observations of the spectral clear-sky aerosol forcing over the tropical Indian Ocean. *JGR Atmos.* **1999**, *104* (D20), 24359-24370. DOI: Doi 10.1029/1999jd900502.

[49] Redemann, J.; Pilewskie, P.; Russell, P. B.; Livingston, J. M.; Howard, S.; Schmid, B.; Pommier, J.; Gore, W.; Eilers, J.; Wendisch, M. Airborne measurements of spectral direct aerosol radiative forcing in the Intercontinental chemical Transport Experiment/Intercontinental Transport and Chemical Transformation of anthropogenic pollution, 2004. *JGR Atmos.* **2006**, *111* (D14). Artn D14210, DOI: 10.1029/2005jd006812.

[50] Ramana, M. V.; Ramanathan, V. Abrupt transition from natural to anthropogenic aerosol radiative forcing: Observations at the ABC-Maldives Climate Observatory. *JGR Atmos.* **2006**, *111* (D20). Artn D20207, DOI: 10.1029/2006jd007063.

[51] Satheesh, S. K.; Ramanathan, V. Large differences in tropical aerosol forcing at the top of the atmosphere and Earth's surface. *Nature* **2000**, *405* (6782), 60-63. DOI: 10.1038/35011039.

[52] Myhre, G.; Samset, B. H.; Schulz, M.; Balkanski, Y.; Bauer, S.; Berntsen, T. K.; Bian, H.; Bellouin, N.; Chin, M.; Diehl, T.; et al. Radiative forcing of the direct aerosol effect from AeroCom Phase II simulations. *ACP* **2013**, *13* (4), 1853-1877. DOI: 10.5194/acp-13-1853-2013.

[53] Schmale, J.; Sharma, S.; Decesari, S.; Pernov, J.; Massling, A.; Hansson, H.-C.; von Salzen, K.; Skov, H.; Andrews, E.; Quinn, P. K.; et al. Pan-Arctic seasonal cycles and long-term trends of aerosol properties from 10 observatories. *ACP* **2022**, *22* (5), 3067-3096. DOI: 10.5194/acp-22-3067-2022.